ORIGINAL ARTICLE

OPEN ACCESS

Artificial Neural Network for Simulation of Friction Drag and Heat Transfer Enhancement in non-Newtonian Nanofluid flow over a Circular Cylinder: Non-similar Solution.

Muhammad Shoaib [1], **Muhammad Imran Khan** [2], **M. Israr-ur-Rehman** [3]

Authors' Affiliation:

[1,2] Department of Mathematics and Statistics, FS, International Islamic University (IIU), Islamabad, Pakistan.
Email: m.shoaib.info@gmail.com
[3] School of Mathematics and Statistics, Central South University, Changsha, China
Email: ibrarg1708@gmail.com

Article History:

Submitted: August 09, 2025
Revised: December 14, 2025
Accepted: December 19, 2025
Published online: Dec 30, 2025

Corresponding author(s):

M. Israr-ur-Rehman
Email: ibrarg1708@gmail.com

ABSTRACT

The primary purpose of the investigation is to highlight the significance of artificial intelligence and machine learning techniques in engineering and fluid mechanics problems. With the advancement in Artificial Intelligence (AI) and Machine Learning (ML) techniques, the computational efficiency and accuracy of numerical results have enhanced. The present study aims to examine MHD boundary layer flow of Casson Nanofluids (CNFs) over a cylinder with thermal radiation effects. Tiwari and Das' model is used to develop a governing Casson nanofluid problem that contains nonlinear PDEs. ANN and numerical models are utilized to examine the effect of numerous physical parameters on heat and fluid transfer properties. The Keller-Box technique, a second-order accurate implicit finite difference scheme, is used to computationally solve the modified fundamental differential equations. However, the predicted solution is examined with MLP-ANN. An efficiency of the proposed model is examined with MSE, correlation index R, and the optimal curve fitness function. An optimal performance of MLP-ANN is examined with the computation of MSE [2.56×10^{-8}, 4.8×10^{-8}, 4.42×10^{-8}, 3.23×10^{-8} and 4.81×10^{-8}] is attained against the epoch [1000, 608, 555, 822, and 787] for scenarios 1-5 with case 1. Graphs and tables illustrate how the Nusselt number ($Gr^{-\frac{1}{5}} Nu$) and skin friction ($Gr^{\frac{1}{5}} C_f$) affect several physical variables related to the Casson nanofluid flow. One of the most important conclusions is that $Gr^{\frac{1}{5}} C_f$ decreases and $Gr^{-\frac{1}{5}} Nu$ increases when the Casson parameter increases.

Keywords: Casson fluid, Thermal radiation, Artificial neural network, Implicit finite difference scheme.

(MSC2020) Codes: 76A05, 80A20, 68T07,65M06

1 | INTRODUCTION

Historically, fluid mechanics has collaborated with massive quantities of data from observations in the field, large-scale computational models, and tests. In fact, high-performance computational platforms and improvements in experimental measuring proficiencies have made big data a reality in fluid mechanics research over the last few decades [1],[2]. However, computational algorithms, predictive modeling, and domain knowledge have been heavily dependent upon in the processing of fluid mechanics data. Fluid mechanics problems ranging from reduced-order modeling, experimental data manufacturing, optimization, turbulence closure simulation, and control may all be tackled with a machine learning (ML) framework. There is a link between the development and applications of numerical methods to solve fluid dynamics equations in the 1940s and 1950s and the current change in scientific research from fundamental principles to data-driven approaches. Machine learning schemes can be beneficial for fluid mechanics, but it also poses obstacles that could lead to additional advancements in the field, complementing engineering intuition and human understanding [3]. It's critical to strike a balance between the excitement surrounding machine learning's potential and the fact that the subject of fluid mechanics is still developing and requires significant work. We also emphasize the advantages of using domain expertise in fluid dynamics to learning algorithms in this scenario. We see the fluid mechanics community playing a similar role to what the numerical techniques community did in the last century in contributing to ML advancements.

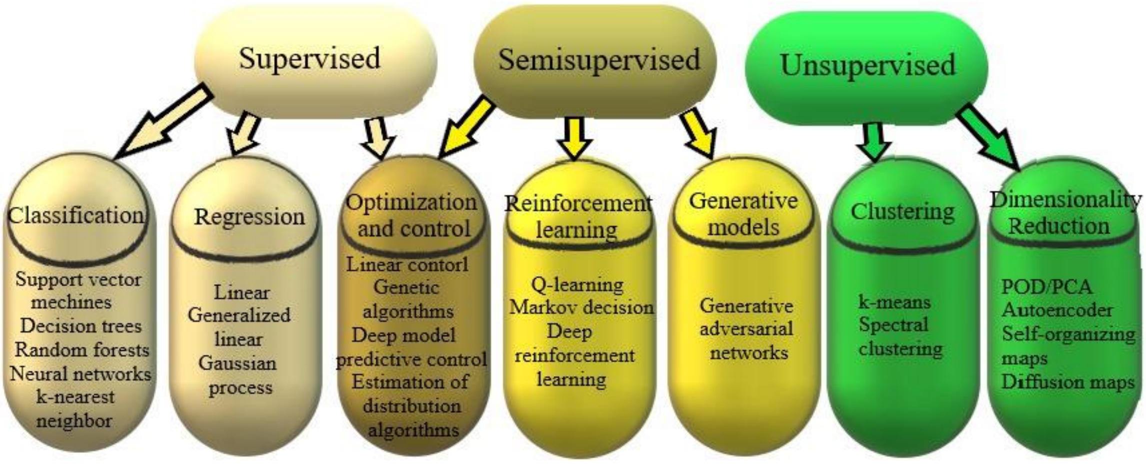

Figure 1. Categorization of Machine Learning Algorithms.

Artificial neural network also an important part of machine learning algorithms. ANNs possess the same structure as the neural architecture found in human brains. ANNs consist of several neurons. These neurons carry information from one part of ANNs to another part of ANNs via a special type of function known as an activation function. There are numerous types of ANNs, i.e., Perceptron, Feed-Forward Neural Networks (FFNN), Conventional Neural Networks (CNN), and

Feed-Back Neural Networks (FBNN). The applications of ANNs span a wide array of fluid dynamics challenges, including modelling boundary layer wind tunnel conditions, resolving issues related to viscous and thermal boundary layers, and addressing singular perturbation problems with thin boundary layers. Due to the wide range of applications of AI and ML, several researchers pay attention to understanding these techniques and applying them in fluid mechanics research. The wall pressure of turbulent boundary layer flow with ANNs was examined by [4]. The application of an active boundary layer had been examined by [5]. They used ANN-based simulation techniques to find the approximate solution. The data driven approach used by [6] of ML to examine the velocity field of turbulent boundary layer flow. The applications of ANNs span a wide array of fluid mechanics challenges, including modelling boundary layer wind tunnel conditions, resolving issues related to viscous and thermal boundary layers, and addressing singular perturbation problems with thin boundary layers [7], [8]. An AI-based technique, ANNs with the LMS-BPNN approach used [9], to investigate the thermal analysis of MHD Casson fluid over a porous surface. [10] used the concepts of [9] to determine the smart solution of boundary layer flow. An ANN with backpropagation was applied to find an approximate solution of viscous fluid over a cylinder [11]. Similarly, [12] explained the application of ML in fluid mechanics. Additionally, [13] examined a large eddy simulation model with artificial neural network techniques. The entropy generation of MHD Cross-nanofluid with artificial neural networks investigated by [14]. Some other recent studies can be seen in [15], [16], [17], [18], [19], [20], [21], [22] and therein.

Non-Newtonian fluid with convective heat transfer over a cylinder holds significant importance due to its wide range of applications in various fields, i.e., pharmaceuticals, chemical processing, cosmetics, food processing, like pasteurization and sterilization processes, ensuring food safety and quality, the petroleum industry, cooling tower, and nuclear reactor, etc. The wide range of these applications has motivated scholars to focus their attention on investigating the boundary layer flow of non-Newtonian fluid and convective heat transfer phenomena. There are different non-Newtonian fluid models have been developed so far, i.e., Carreau-fluid [23], Carreau-Yasuda fluid [24], Powell-Eyring fluid [25], Williamson fluid [26], and Casson fluid model [27]. The interesting phenomena of mixed convection flow of micropolar fluid over a cylinder were analyzed by [28]. The numerical investigation of the boundary layer flow of non-Newtonian fluid over a cylinder was analysed by [29].

The thermal characteristics of the fluid are enhanced with an increment of nanoparticles. In many common fluids, i.e., kerosene oil, water, ethylene glycol, etc., two different nanoparticles are used to structure hybrid nanofluids. The nanoparticles dispersed within the base fluids significantly boost the thermal conductivity of the hybrid fluid. This enhancement plays a key role in enhancing heat transfer mechanisms, thus strengthening the fluid's applicability across various engineering and industrial applications. [30] investigated improved thermal characteristics in the flow of a hybrid nanofluid over a channel with graphene/Fe_3O_4 nanoparticles. The heat transfer analysis in unsteady MHD flow of ternary hybrid Casson fluid over an elongating disk with thermal radiation effects inspected by [31]. The MHD unsteady boundary layer flow of Casson hybrid nanofluid (HNF) over a porous shrinking/stretching sheet examined by [32]. The instability of tri-hybrid nanofluid over a porous medium with thermal radiation effects explored in study [33] . Other fascinating applications of thermal radiation with nanofluid can be found in ref. [34], [35], [36], [37], [38], [39], [40].

2 | PROBLEM FORMULATION

Convective boundary layer flow over a horizontal circular cylinder in two dimensions, incompressible, and in a steady state, for a non-Newtonian nanofluid based on carbon nanotubes and methanol, with a uniform surface heat flux. q_w. Fig. 2 elaborates on the problem's physical configuration. The curvilinear coordinates $\tilde{x}$ and $\tilde{y}$ are measured along the cylinder's surface and distance normal to the surface, respectively.

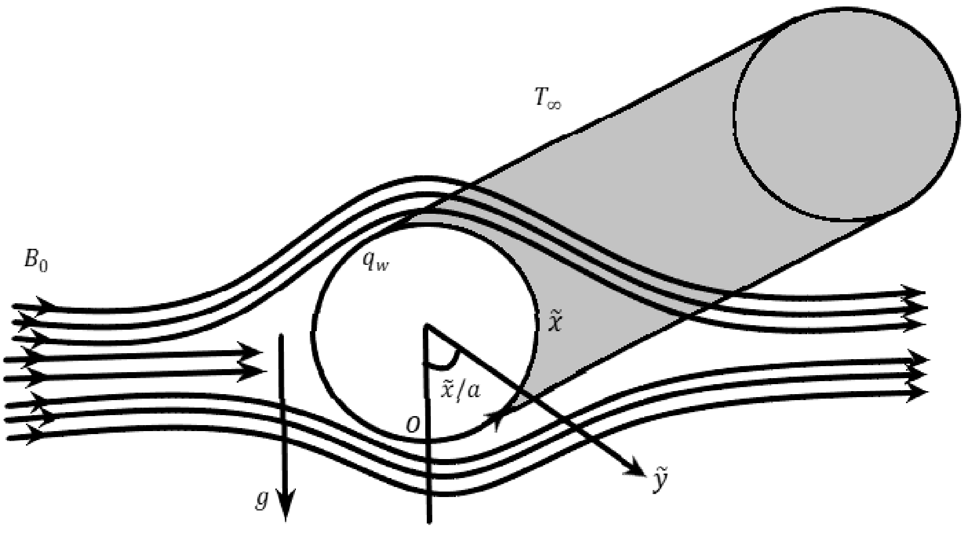

Figure 2. Flow geometry.

Under the assumption of boundary layer approximation and an application of the Tiwari-Das model, the flow problem contains nonlinear Partial Differential Equations (PDEs). The following PDEs are defined [3], [5], [15], [31];

$$\frac{\partial \hat{u}}{\partial \hat{x}} + \frac{\partial \hat{v}}{\partial \hat{y}} = 0, \tag{1}$$

$$\hat{u}\frac{\partial \hat{u}}{\partial \hat{x}} + \hat{v}\frac{\partial \hat{u}}{\partial \hat{y}} = v_{nf}\left(1+\frac{1}{\gamma}\right)\frac{\partial^2 \hat{u}}{\partial \hat{y}^2} + \left(\frac{\chi\rho_s\beta_s + (1-\chi)\rho_f\beta_f}{\rho_{nf}}\right)g(T-T_\infty)\sin\left(\frac{\hat{x}}{a}\right) - \frac{\alpha_{nf}B_0^2}{\rho_{nf}}\hat{u}, \tag{2}$$

$$\left(\hat{u}\frac{\partial T}{\partial \hat{x}}+\hat{v}\frac{\partial T}{\partial \hat{y}}\right)=\alpha_{nf}\frac{\partial^2 T}{\partial \hat{y}^2}+\frac{16}{3(\rho c_p)_{nf}}\frac{\sigma^*}{k^*}T_\infty^3\frac{\partial^2 T}{\partial \hat{y}^2}+ \frac{\mu_{nf}}{(\rho c_p)_{nf}}\left(1+\frac{1}{\gamma}\right)\left(\frac{\partial \hat{u}}{\partial \hat{y}}\right)^2+\frac{\alpha_{nf}B_0^2}{\rho_{nf}}(\hat{u})^2. \tag{3}$$

Boundary conditions for the proposed flow situation are;

$$\hat{u}(\hat{x},\hat{y})=\hat{v}(\hat{x},\hat{y})=0,\frac{\partial T(\hat{x},\hat{y})}{\partial \hat{y}}=-\frac{q_w}{k},\ \text{at}\ \hat{y}=0$$
$$\hat{u}(\hat{x},\hat{y})\to 0, T(\hat{x},\hat{y})\to T_\infty, \text{as}\ \hat{y}\to\infty. \tag{4}$$

Tiwari-Das model for nanoparticles is [15];

$$\frac{\alpha_{nf}}{\alpha_f}=1+\frac{3(\sigma-1)\chi}{(\sigma+2)-(\sigma-1)\chi'},\sigma=\frac{\sigma_s}{\sigma_f},\frac{k_{nf}}{k_f}=\frac{(k_s+2k_f)-2\chi(k_f-k_s)}{(k_s+2k_f)+\chi(k_f-k_s)},$$
$$\mu_{nf}=\frac{\mu_f}{(1-\chi)^{2.5}},(\rho c_p)_{nf}=(1-\chi)\rho_f+\chi\rho_s,\alpha_{nf}=\frac{k_{nf}}{(\rho c_p)_{nf}}, \tag{5}$$

The dimensionless variables are addressed as follows [5];

$$x=\frac{\hat{x}}{a},y=Gr^{\frac{1}{5}}\frac{\hat{y}}{a},\bar{u}=\left(\frac{a}{\nu_f}\right)Gr^{\frac{1}{5}}\hat{u},\bar{v}=\left(\frac{a}{\nu_f}\right)Gr^{-\frac{2}{5}}\hat{v},\bar{\theta}=Gr^{\frac{1}{5}}\left(\frac{T-T_\infty}{aq_w/k_f}\right), \tag{6}$$

The dimensionless equations are obtained by applying equation (6) to differential equations $(1-4)$.

$$\frac{\partial \bar{u}}{\partial x}+\frac{\partial \bar{v}}{\partial y}=0, \tag{7}$$

$$\bar{u}\frac{\partial \bar{u}}{\partial x}+\bar{v}\frac{\partial \bar{u}}{\partial y}=\frac{\rho_f}{(1-\chi)^{2.5}}\left(1+\frac{1}{\gamma}\right)\frac{\partial^2 \bar{u}}{\partial y^2}+\left(\frac{\frac{\chi\rho_s\beta_s}{\beta_f}+(1-\chi)\rho_f}{\rho_{nf}}\right)\bar{\theta}\sin x- \frac{\sigma_{nf}\rho_f}{\sigma_f\rho_{nf}}Mu, \tag{8}$$

$$\left(\bar{u}\frac{\partial \bar{\theta}}{\partial x}+\bar{v}\frac{\partial \bar{\theta}}{\partial y}\right)=\frac{1}{Pr}\left(\frac{k_{nf}}{k_f}+Rd\right)\frac{(\rho c_p)_f}{(\rho c_p)_{nf}}\frac{\partial^2 \bar{\theta}}{\partial y^2}+ Ec\frac{\mu_{nf}}{\mu_f}\frac{(\rho c_p)_f}{(\rho c_p)_{nf}}\left(1+\frac{1}{\gamma}\right)\left(\frac{\partial \bar{u}}{\partial y}\right)^2+J\frac{\sigma_{nf}}{\sigma_f}\frac{(\rho c_p)_f}{(\rho c_p)_{nf}}(\bar{u})^2, \tag{9}$$

Boundary conditions are transformed as follows;

$$\bar{v}=0,\quad \bar{u}=0,\quad \frac{\partial\bar{\theta}}{\partial y}=-1,\quad \text{at}\ y=0,$$
$$\bar{u}\to 0,\quad \bar{\theta}\to 0,\quad \text{as}\ y\to\infty, \tag{10}$$

The dimensionless parameters appear in Eqns. (8-9) are; $M=\left(\frac{\sigma_f B_0^2 Gr^{-\frac{2}{5}}}{\rho_f\nu_f}\right)$ is the magnetic parameter, $Rd=\frac{16}{3}\frac{\sigma^*}{k^*k_f}T_\infty^3$ is a thermal radiation parameter, $Gr=\frac{g\beta_f(T_w-T_\infty)a^3}{\nu_f^2}$ is the Grashof number, $J=\frac{\sigma_f\nu_f B_0^2 Gr^{\frac{3}{5}}}{(\rho c_p)_f a q_w/k_f}$ is Joule heating parameter, $Ec=\frac{\rho_f\nu_f^2 Gr}{(\rho c_p)_f a^3 q_w/k_f}$ is the Eckert number and $\Pr=\frac{\nu_f}{\alpha_F}$ is the Prandtl number. Because of their nonlinearity and numerous dependent variables, PDEs as specified in Equations (7) through (10) are challenging to solve. Consequently, take into account the following transformations:

$$\bar{u} = \frac{\partial\psi}{\partial\eta}, \bar{v} = -\frac{\partial\psi}{\partial\eta}, \psi = \xi\tilde{f}(\xi,\eta), \bar{\theta} = \tilde{\theta}(\xi,\eta), \text{ and } \xi = \bar{x}, \eta = \bar{y}, \tag{11}$$

Here $\bar{u} = \frac{\partial\psi}{\partial\eta}$, and $\bar{v} = -\frac{\partial\psi}{\partial\xi}$, ψ is the stream function. We apply Eqn. (11) to transform Eqns. (7) − (10) as follow;

$$\frac{\rho_f}{(1-\chi)^{2.5}\rho_{nf}}\left(1+\frac{1}{\gamma}\right)\frac{\partial^3\tilde{f}}{\partial\eta^3} - \left(\frac{\partial\tilde{f}}{\partial\eta}\right)^2 + \tilde{f}\frac{\partial^2\tilde{f}}{\partial\eta^2} + \left(\frac{\frac{\chi\rho_s\beta_s}{\beta_f} + (1-\chi)\rho_f}{(1-\chi)\rho_f + \chi\rho_s}\right)\tilde{\theta}\frac{Sin\xi}{\xi} - \frac{\sigma_{nf}\rho_f}{\rho_f\rho_{nf}}M\frac{\partial\tilde{f}}{\partial\eta} = \xi\left(\frac{\partial\tilde{f}}{\partial\eta}\frac{\partial^2\tilde{f}}{\partial\xi\partial\eta} - \frac{\partial\tilde{f}}{\partial\xi}\frac{\partial^2\tilde{f}}{\partial\eta^2}\right), \tag{12}$$

$$\frac{1}{Pr}\left(\frac{k_{nf}}{k_f} + Rd\right)\frac{(\rho c_p)_f}{(\rho c_p)_{nf}}\frac{\partial^2\tilde{\theta}}{\partial\eta^2} + \tilde{f}\frac{\partial\tilde{\theta}}{\partial\eta} + Ec\xi^2\frac{\mu_{nf}}{\mu_f}\frac{(\rho c_p)_f}{(\rho c_p)_{nf}}\left(1+\frac{1}{\gamma}\right)\left(\frac{\partial^2\tilde{f}}{\partial\eta^2}\right)^2 + J\xi^2\frac{\sigma_{nf}}{\sigma_f}\frac{(\rho c_p)_f}{(\rho c_p)_{nf}}\left(\frac{\partial\tilde{f}}{\partial\eta}\right)^2 = \xi\left[\frac{\partial\tilde{f}}{\partial\eta}\frac{\partial\tilde{\theta}}{\partial\xi} - \frac{\partial\tilde{f}}{\partial\xi}\frac{\partial\tilde{\theta}}{\partial\eta}\right], \tag{13}$$

Boundary conditions in the form of new variables are;

$$\frac{\partial\tilde{f}(\xi,\eta)}{\partial\eta} = 0, \quad \tilde{f}(\xi,\eta) = 0, \quad \frac{\partial\tilde{\theta}(\xi,\eta)}{\partial\eta} = -1, \quad \text{at } \eta = 0,$$
$$\frac{\partial\tilde{f}(\xi,\eta)}{\partial\eta} \to 0, \quad \tilde{\theta}(\xi,\eta) \to 0, \quad \text{as } \eta \to \infty, \tag{14}$$

The flow outcomes are skin friction (C_f) and Nusselt number (Nu) are [5,18];

$$C_f = \frac{\tau_w}{\rho U_\infty^2}, \qquad Nu = \frac{aq_w}{k_f(T_s - T_\infty)}, \tag{15}$$

where τ_w is surface shear stress, q_w is surface heat flux, and $T_s = T_\infty + \tilde{\theta}(\xi,0)Gr^{-1/5}\frac{aq_w}{k_f}/(\frac{k_{nf}}{k_f} + Rd)$ is surface temperature [19]:

$$Gr^{\frac{1}{5}}C_f = \frac{1}{(1-\chi)^{2.5}}\left(1+\frac{1}{\gamma}\right)\left(\xi\frac{\partial^2\tilde{f}(\xi,0)}{\partial\eta^2}\right)_{\eta=0}, Gr^{-1/5}Nu = \left(\frac{k_{nf}}{k_f} + Rd\right)\left(\frac{1}{\tilde{\theta}(\xi,0)}\right) \tag{16}$$

3 | NUMERICAL METHOD

Non-linear PDEs (13-15) are numerically solved using the Keller-box technique, an implicit finite difference scheme. Subject to the boundary conditions (14). Some of the early studies that used the Keller-box approach to solve non-linear DEs and PDEs are found in works [27], [28], [29]. To obtain the numerical result for the system of equations, four crucial steps can be taken:

I. The leading partial differential equations are first converted into first-order partial differential equations.
II. Utilizing the central difference approximation and average values, rewrite the resultant equations.

III. Transformed the algebraic equations into matrix-vector form after linearizing them

IV. The matrix equations are solved using the block-tridiagonal-elimination method.

To transform the system of differential equations (12–13) into first-order differential equations, the subsequent variables are added, according to the boundary conditions (14).

$$\check{F} = \check{f}, \check{\theta} = \check{s},, \check{f}' = \check{u}, \check{u}' = \check{v}, \check{s}' = \check{t}, \tag{17}$$

Then, the transformed equation becomes

$$\xi\left[\check{u}\frac{\partial \check{u}}{\partial \xi} - \check{v}\frac{\partial \check{f}}{\partial \xi}\right] = A\check{v}' + \check{f}\check{v} - \check{u}^2 + C\check{u} + B\check{s}\frac{\sin\xi}{\xi}, \tag{18}$$

$$\xi\left[\check{u}\frac{\partial \check{s}}{\partial \xi} - \check{t}\frac{\partial \check{f}}{\partial \xi} - \xi D\check{v}^2\right] = \frac{E}{\mathrm{Pr}}\check{t}' + \check{f}\check{t} + H\check{u}^2, \tag{19}$$

with boundary condition

$$\begin{aligned} &\check{f}(\xi,\eta) = 0, \check{u}(\xi,\eta) = 0, \check{t}(\xi,\eta) = -1, \text{at } \eta = 0 \\ &\check{u}(\xi,\eta) \to 0, \check{s}(\xi,\eta) \to 0, \qquad as\ \eta \to \infty. \end{aligned} \tag{20}$$

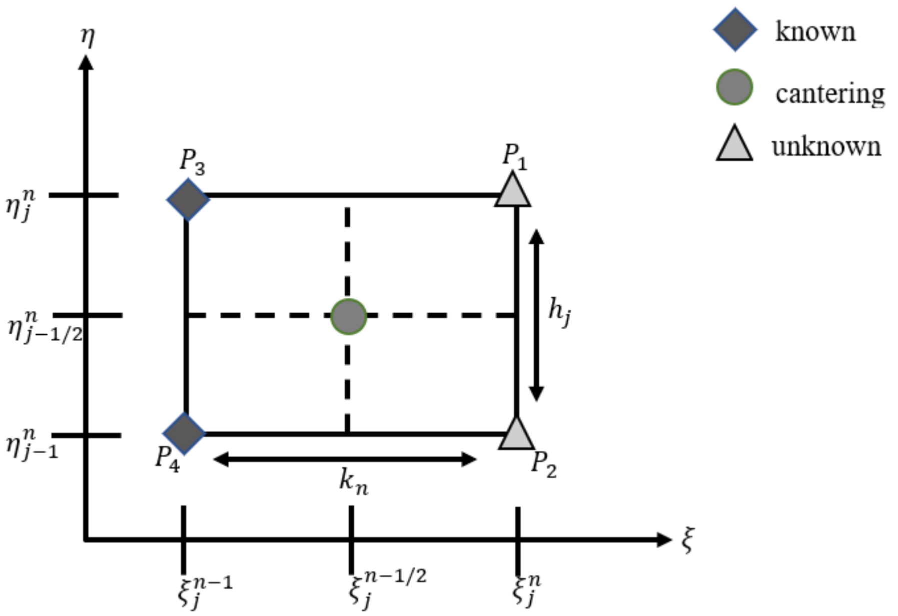

Figure 3. Net rectangle used for difference approximations

Figure 2 displays the net rectangle under the ξ and η planes under consideration. Equation (21) specifies the net points.

$$\begin{aligned} \xi^n &= \xi^{n-1} + k_n, & n &= 1, 2, \ldots, I, \\ \eta_j &= \eta_{j-1} + h_j, & j &= 1, 2, \ldots, J, \\ x^0 &= 0, \quad \eta^0 = 0, & \eta_J &= \eta_\infty, \end{aligned} \tag{21}$$

where k_n and h_j is the step size along ξ and η directions, respectively.

$$\frac{\partial(-)}{\partial\xi} = \frac{1}{k_n}\left[(-)_j{}^n - (-)_j{}^{n-1}\right], \frac{\partial(-)}{\partial\eta} = \frac{1}{h_j}\left[(-)_j{}^n - (-)_{j-1}{}^n\right],$$
$$(-)_j^{n-\frac{1}{2}} = \frac{1}{2}\left[(-)_j^n + (-)_j^{n-1}\right], \text{and } (-)_{j-\frac{1}{2}}^n = \frac{1}{2}\left[(-)_j^n + (-)_{j-1}^n\right]. \tag{22}$$

Table 1: Comparison of the computed skin friction coefficient ($Gr^{\frac{1}{5}}C_f$) at various numerical values of ξ when $\Pr = 1, \chi = Rd = J = Ec = M = 0$, and $\gamma \to \infty$ with the results available in the literature.

ξ	**Merkin et al. [3]**	**Molla et al. [5]**	**Present**
0.0	0.000	0.000	0.0000
0.2	0.274	0.272	0.2726
0.6	0.795	0.789	0.7925
1.0	1.241	1.226	1.2371
1.6	1.671	1.637	1.6642
2.0	1.744	1.693	1.7393
2.6	1.451	1.370	1.4392
π	0.613	0.585	0.5734

Table 2: Comparison of the computed $\theta(\xi, 0)$ at various numerical values of ξ when $\Pr = 1, \chi = Rd = J = Ec = M = 0$, and $\gamma \to \infty$ with the results available in the literature.

ξ	**Merkin et al. [3]**	**Molla et al. [5]**	**Present**
0.0	1.996	1.996	1.996
0.2	1.999	1.999	1.998
0.6	2.014	2.015	2.012
1.0	2.043	2.047	2.042
1.6	2.120	2.129	2.120
2.0	2.202	2.216	2.203
2.6	2.403	2.430	2.406
π	2.824	2.824	2.851

3.1 Artificial Neural Network Design

The objective is to apply the ANN scheme on a non-Newtonian nanofluid past a horizontal cylinder and analyse the flow behaviour and heat transfer phenomena. In Computational Fluid Dynamics (CFD), Artificial Neural Networks (ANNs) are a highly useful and efficient technique for the simulation of non-Newtonian flow behaviour. An ANN creates a Multilayered Perceptron (MLP), while an MLP is a network that connects various layers. For each variable, there are different algorithms of MLP-ANN. In MLP-ANN frameworks algorithm optimizes the data set with some mathematical functions, i.e., activation function. The MLP-ANN methods' prediction performance is based on data optimization [30]. The network model has been trained to optimize data, and its accuracy in predicting algorithms has been studied. The network model is run to get the expected valuation once the MLP-ANN technique has trained. Figure 4 shows an essential flowchart utilized in the design of MLP-ANN systems. The Feed-Forward Neural Network (FFNN) and Back-Propagation (BP) Multilayered Perceptual (MLP) network topologies are two of the most used in the proposed MLP-ANN approach because of their complex configurations. The first layer of the MLP system is known as the input layer; the second layer is known as the hidden layer; and the third layer is known as the output layer. In this network, a weighted neuron is entered (input) in the second hidden layer. The neuron signal then proceeded to the input layer and passed to the hidden layer with different topologies, a major component that makes decisions (output), after the hidden layer. In MLP, each layer is interconnected. Information transmitted forward from the input layer is returned to the hidden layer in a feed-forward network, which helps to minimize the difference between stated estimates and objective estimates.

Table 3: Valuations of input parameters used in ANN models.

Scenario	Case	Pertained parameter				
		$\boldsymbol{M}$	$\boldsymbol{\gamma}$	$\boldsymbol{Rd}$	$\boldsymbol{J}$	$\boldsymbol{\chi}$
1	1	0.5	0.5	1.5	0.5	0.2
	2	1.0	0.5	1.5	0.5	0.2
	3	2.0	0.5	1.5	0.5	0.2
	4	3.0	0.5	1.5	0.5	0.2
2	1	0.5	0.5	1.5	0.5	0.2
	2	0.5	1.0	1.5	0.5	0.2
	3	0.5	2.0	1.5	0.5	0.2
	4	0.5	3.0	1.5	0.5	0.2
3	1	0.5	0.5	0.0	0.5	0.2
	2	0.5	1.0	0.5	0.5	0.2
	3	0.5	2.0	1.5	0.5	0.2
	4	0.5	3.0	2.0	0.5	0.2
4	1	0.5	0.5	1.5	0.0	0.2
	2	0.5	1.0	1.5	0.5	0.2
	3	0.5	2.0	1.5	1.5	0.2
	4	0.5	3.0	1.5	2.0	0.2
5	1	0.5	0.5	1.5	0.5	0.0
	2	0.5	1.0	1.5	0.5	0.2
	3	0.5	2.0	1.5	0.5	0.4
	4	0.5	3.0	1.5	0.5	0.6

This investigation, which continues while the error rate is reduced, ends when the maximum prediction efficiency is attained, and MLP-ANN methods' training is finished. There is no known, reliable model that can predict the number of neurons in the hidden layer of multilayer perceptron (MLP) networks, so the MLP-ANN scheme with seven neurons in the hidden layer has been demonstrated, and the predictive capabilities of MLP-ANN models constructed with different numbers of neurons have been investigated. Figure 5 shows the physical design of an MLP design. The MLP-ANN technique, which was used to forecast LNN, was developed using the 36 data sets, 70% of the data used for training, 15% for validation, and 15% for testing.

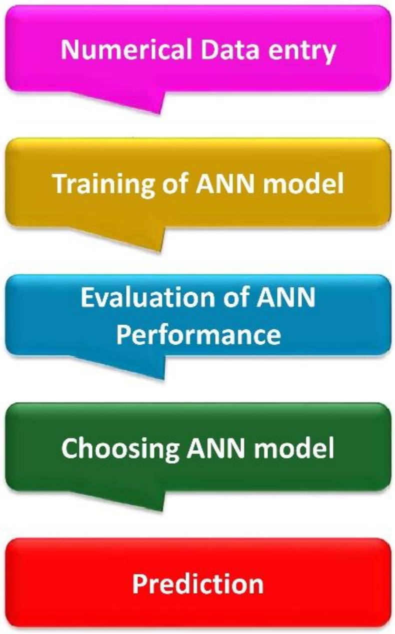

Figure 4. The flow diagram used to create MLP-ANN schemes.

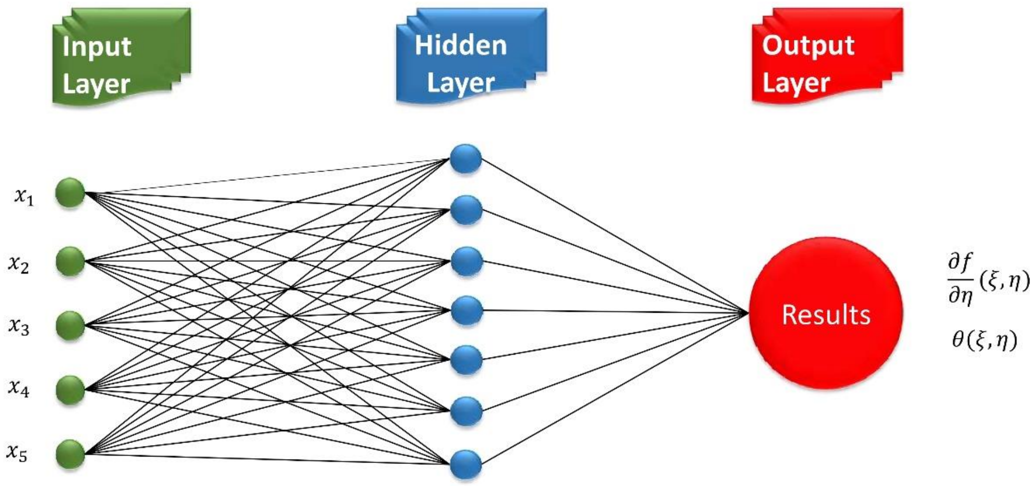

Figure 5. A network's MLP configuration design.

The network models' output and hidden layers, respectively, make use of the Tan-Sig and Purelin [31] transport functions. The mathematical explanations of transport functions are as follows:

$$f(x) = \frac{1}{1+e^{-x}},\ \text{purelin(x)} = \text{x},$$

The next phase in the creation of MLP-ANN schemes is to analyze the prediction accuracy of models. The averaged relative error (ARE), mean square error (MSE), and coefficient of correlation (R) variables have been investigated with MLP-ANN techniques. A list of mathematical methods used to determine the efficacy factors is provided below.

$$MSE = \frac{1}{N}\sum_{i=1}^{N}\left(X_{targ(i)} - X_{ANN(i)}\right)^2, \tag{23}$$

$$R = \sqrt{1 - \frac{\sum_{i=1}^{N}\left(X_{targ(i)} - X_{ANN(i)}\right)^2}{\sum_{i=1}^{N}\left(X_{targ(i)}\right)^2}}, \tag{24}$$

$$Error\ rate\ (\%) = \left[\frac{X_{targ} - X_{ANN}}{X_{targ}}\right] \times 100. \tag{25}$$

Table 4: Analogous analysis with ANN for $Gr^{\frac{1}{5}}C_f$ for scenario 1 of case 1-4.

Scenario	Case	MSE Level			Performance	Gradient	Mu	Epoch
		Training	Validation	Testing				
1	1	2.5615×10^{-8}	8.1585×10^{-8}	3.0847×10^{-8}	2.56×10^{-8}	5.18×10^{-7}	1.0×10^{-9}	1000
	2	3.3202×10^{-8}	6.3864×10^{-8}	7.6875×10^{-7}	3.32×10^{-8}	5.08×10^{-5}	1.0×10^{-9}	658
	3	2.7961×10^{-8}	5.9932×10^{-8}	2.1739×10^{-7}	2.8×10^{-8}	1.10×10^{-7}	1.0×10^{-9}	1000
	4	4.5717×10^{-8}	2.7831×10^{-8}	3.2710×10^{-8}	4.57×10^{-8}	4.86×10^{-8}	1.0×10^{-8}	564

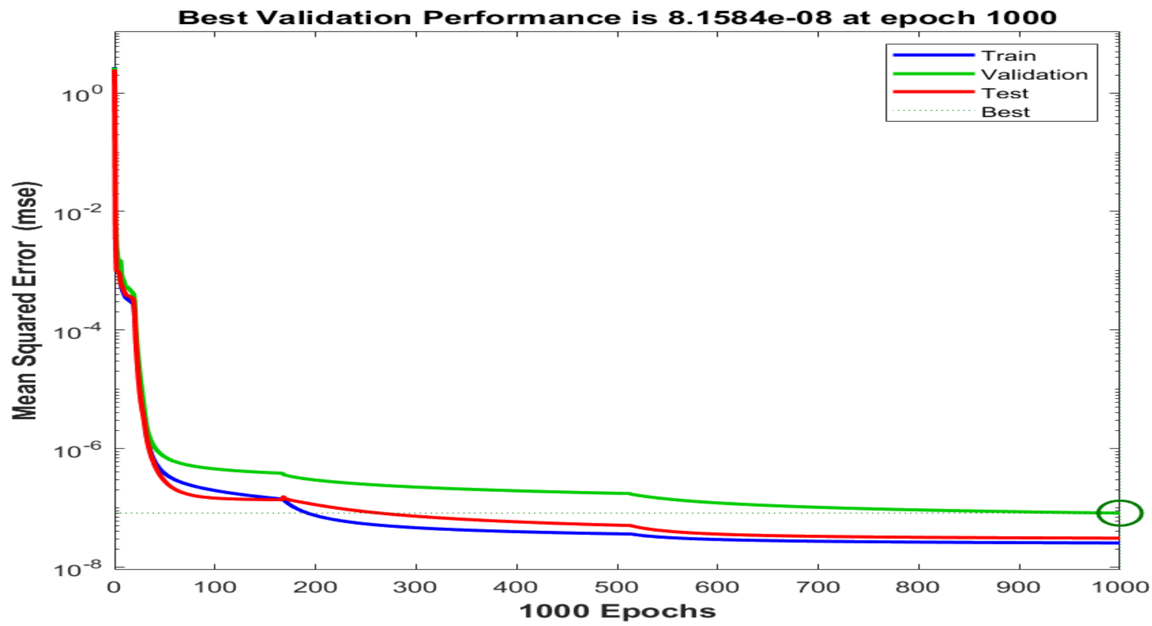

Figure 6(a). Performance of the ANN algorithm in terms of MSE.

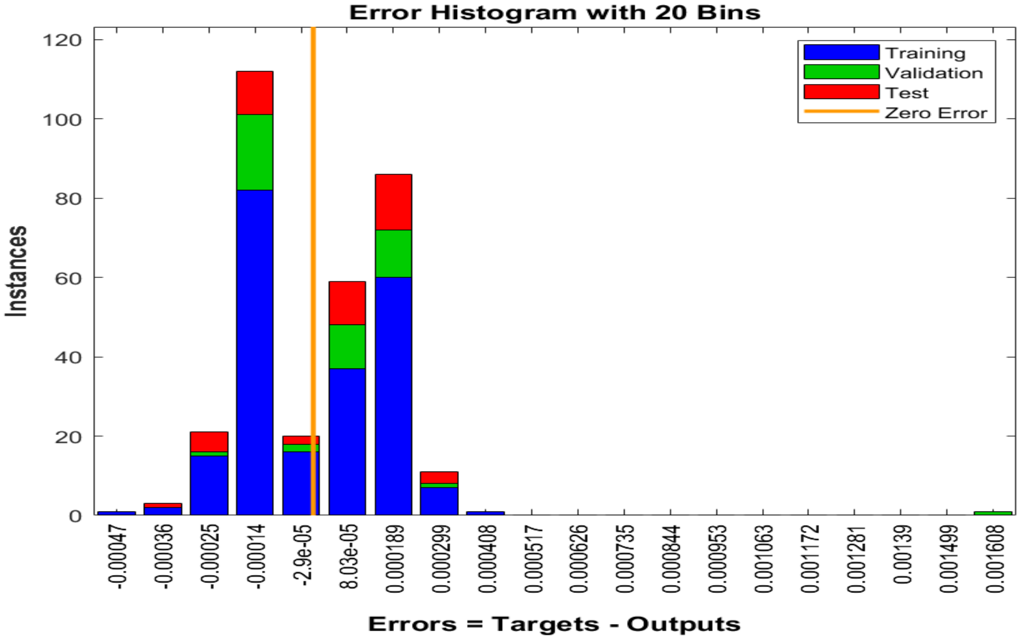

Figure 6(b). Error Histogram of ANN Algorithm.

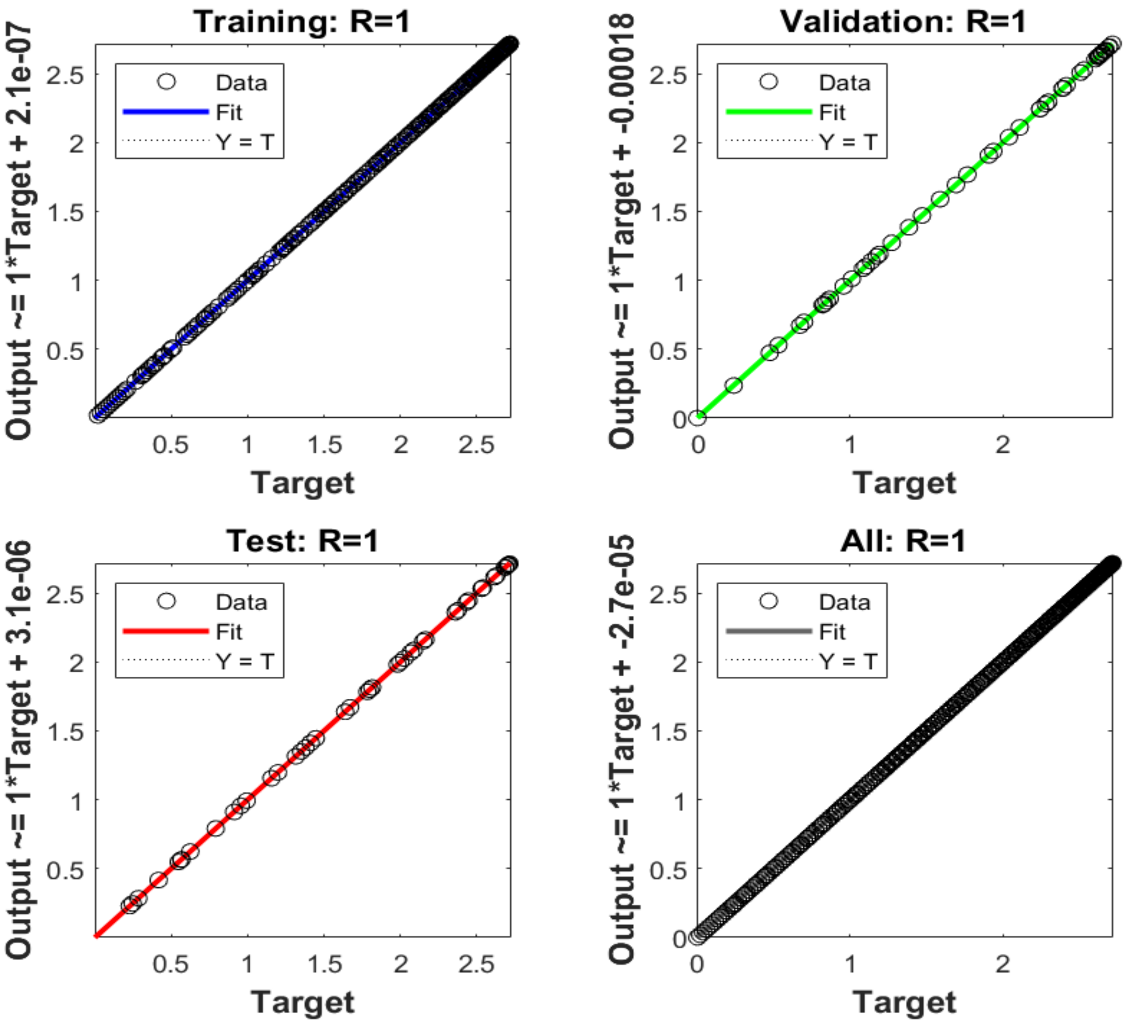

Figure 6(c.). Linear regression of the ANN Algorithm.

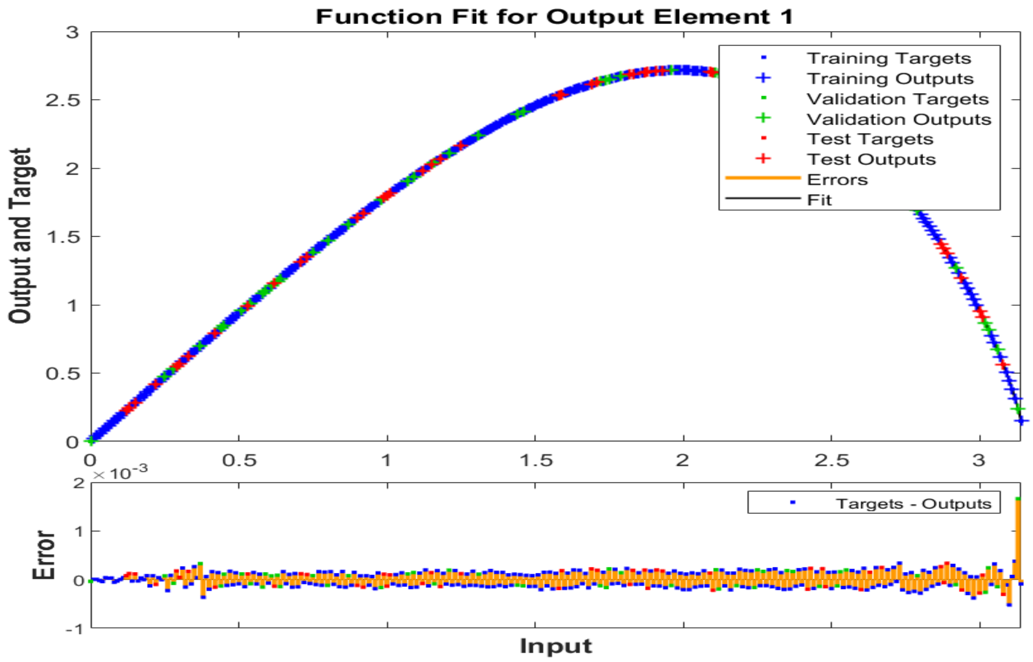

Figure 6 (d). Fitness function maximum curve with ANN Algorithm.

Figure 6 (a-d), graphical representation of the analysis of data for scenario 1 for case 1.

Table 5. Analogous analysis with ANN for $Gr^{\frac{1}{5}}C_f$ for scenario 2 of case 1-4.

Scenario	Case	MSE Level			Performance	Gradient	Mu	Epoch
		Training	Validation	Testing				
2	1	4.7934×10^{-8}	3.0214×10^{-8}	3.4089×10^{-8}	4.8×10^{-8}	4.24×10^{-5}	1.0×10^{-8}	608
	2	1.1002×10^{-8}	2.7433×10^{-8}	1.3202×10^{-8}	1.10×10^{-8}	6.50×10^{-8}	1.0×10^{-9}	1000
	3	8.1496×10^{-9}	1.0128×10^{-8}	2.0306×10^{-8}	8.15×10^{-8}	4.19×10^{-7}	1.0×10^{-9}	1000
	4	1.6314×10^{-8}	1.0677×10^{-8}	8.3124×10^{-9}	1.63×10^{-8}	3.88×10^{-8}	1.0×10^{-8}	1000

4 | RESULTS AND DISCUSSION

The author focusses to scrutinize the flow situation of Casson nanofluid over a cylinder with thermal radiation (Rd). The effects on flow response output are analysed against the parameters of interest, as shown in Table 3. The predicted solution is obtained with ANN based algorithm, i.e., MLP-ANN. The pertinent parameters of interest are displayed in Table 3. Table 4 presents tabulated values of gradient, Mu, and MSE for scenario 1 for different cases 1-4. The performance of MLP-ANN is obtained 2.56×10^{-8}, 3.32×10^{-8}, 2.8×10^{-8}, and 4.5×10^{-8} against epoch 1000, 658, 1000, and 564 for scenario 1 of case 1-4. Numerical values of Mu and gradient for an approximate result of boundary layer characterizing non-Newtonian nanofluid and heat transfer are [1.0×10^{-9}, 1.0×10^{-9} 1.0×10^{-9}, 1.0×10^{-8}] and [5.18×10^{-7}, 5.08×10^{-5}, 1.10×10^{-7} and 4.86×10^{-8}] for scenario 1 of case 1-4, respectively.

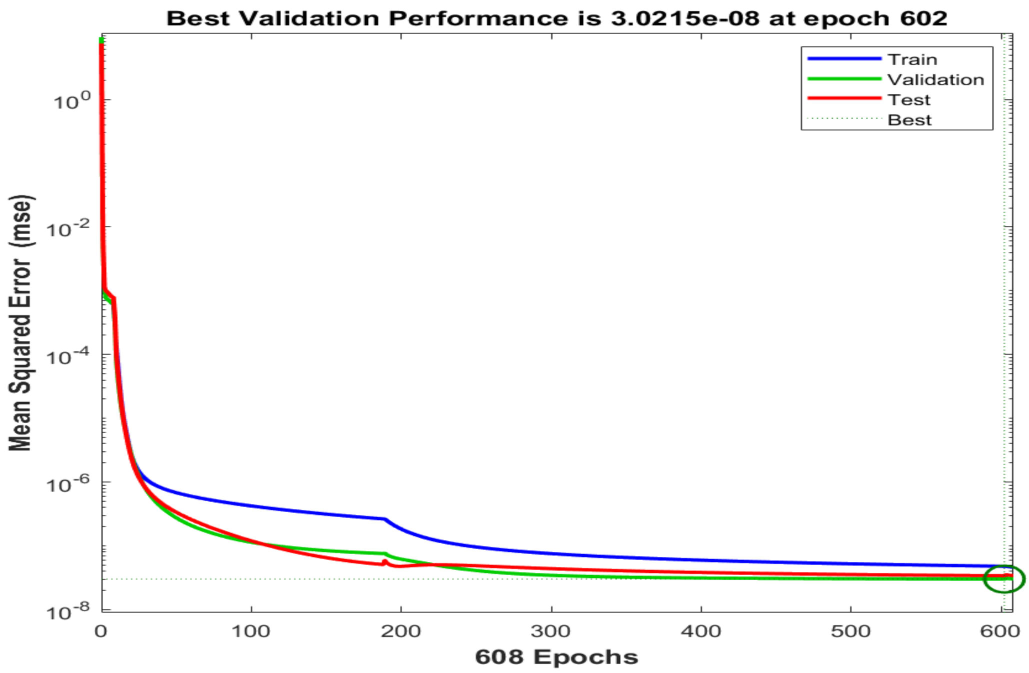

Figure 7(a). Performance of the ANN algorithm in terms of MSE.

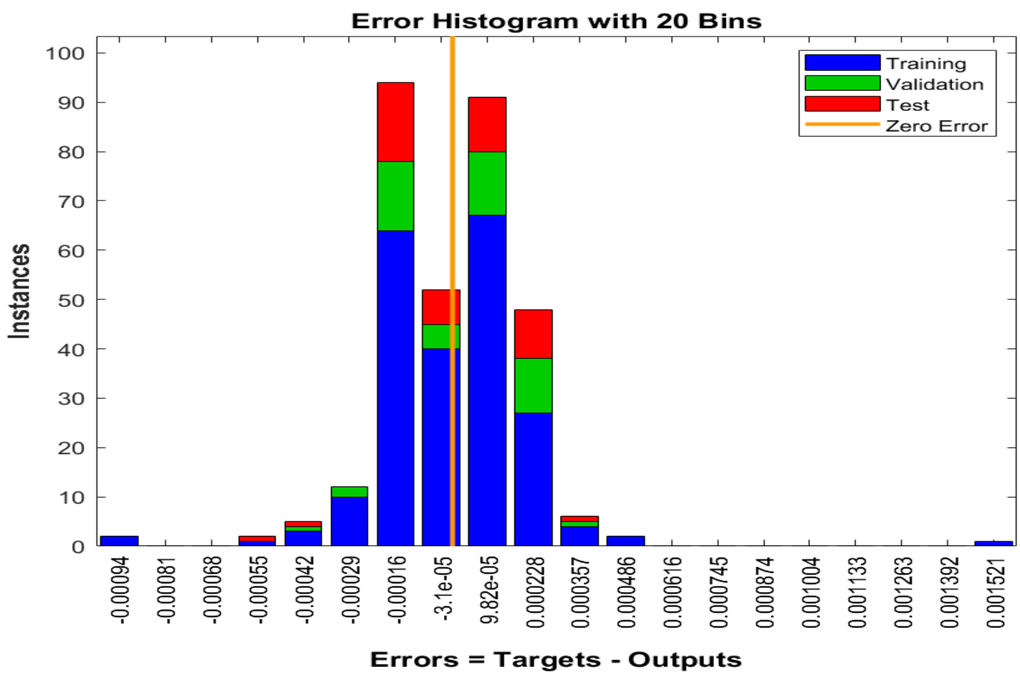

Figure 7(b). Error Histogram of ANN Algorithm.

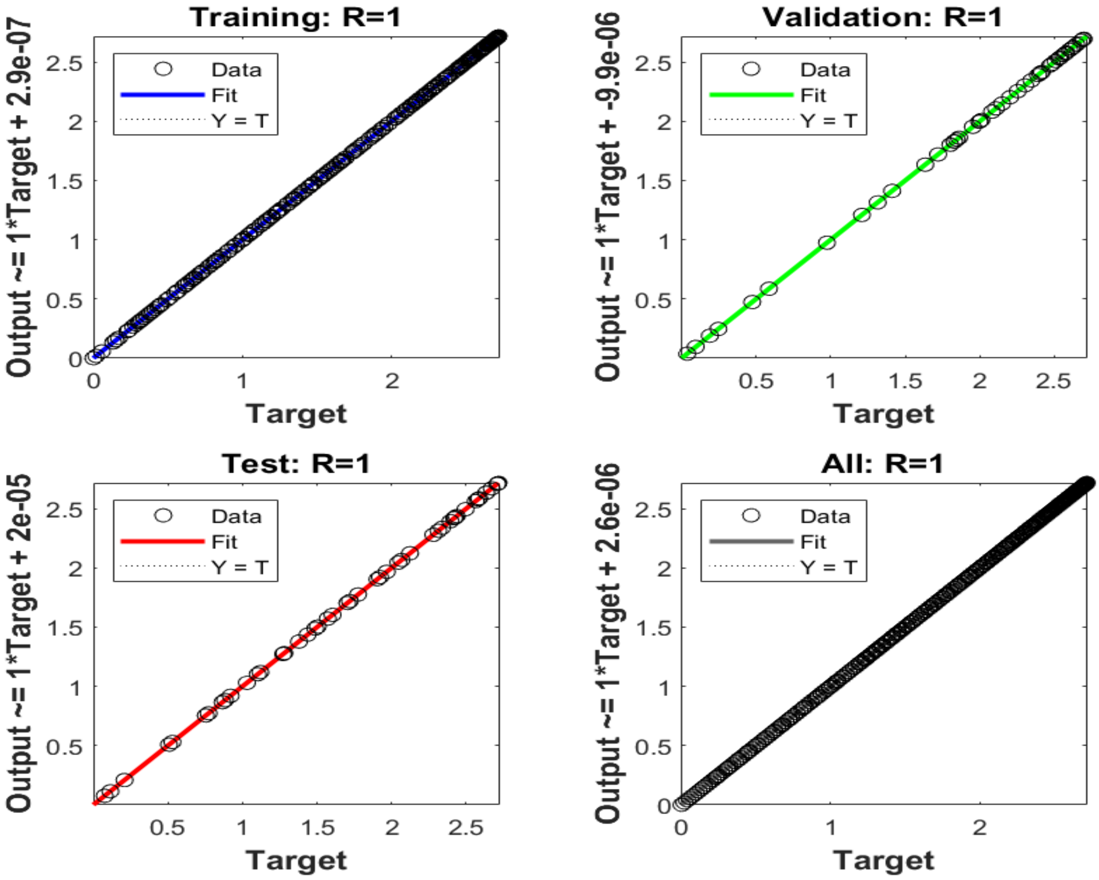

Figure 7c. Linear regression of the ANN Algorithm.

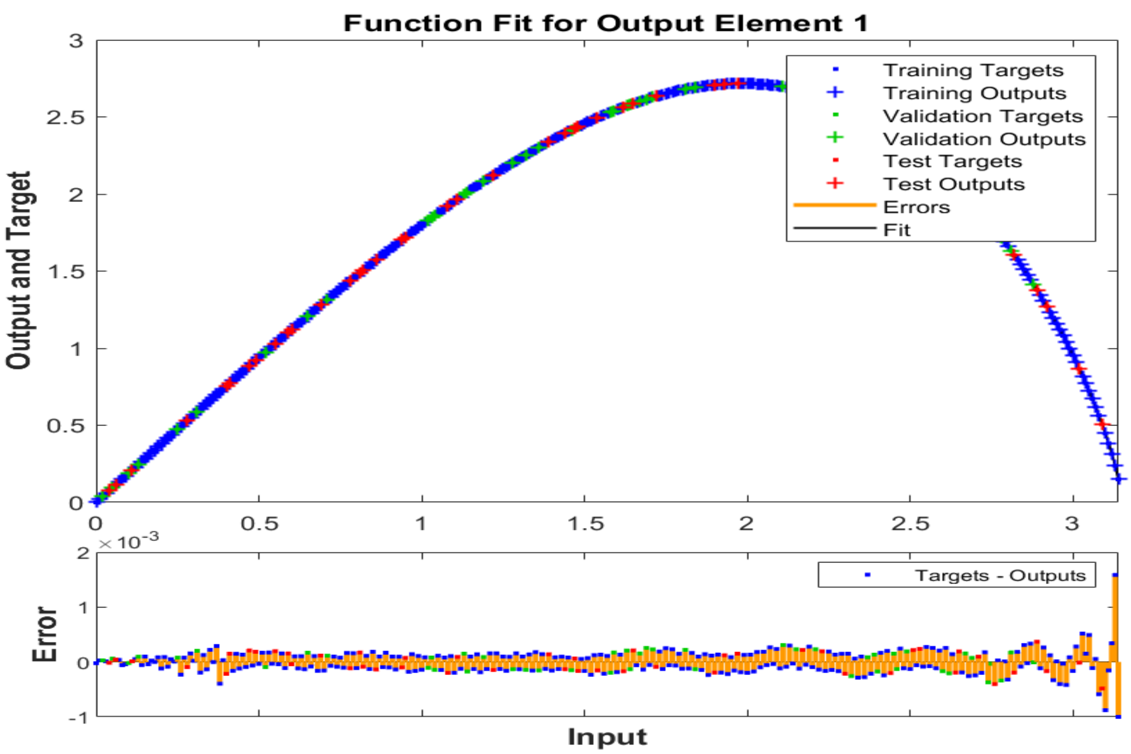

Figure (7d). Fitness function maximum curve with ANN Algorithm

Figure 7(a-d), graphical representation of the analysis of data for scenario 2 for case 1.

Table 6: Analogous analysis with ANN for $Gr^{\frac{1}{5}}C_f$ for scenario 3 of case 1-4.

Scenario	Case	MSE Level			Performance	Gradient	Mu	Epoch
		Training	Validation	Testing				
3	1	4.4277×10^{-8}	2.6340×10^{-8}	3.7080×10^{-8}	4.42×10^{-8}	1.81×10^{-5}	1.0×10^{-9}	555
	2	3.8873×10^{-8}	5.1095×10^{-8}	1.0836×10^{-7}	3.89×10^{-8}	1.97×10^{-7}	1.0×10^{-9}	1000
	3	2.8342×10^{-8}	4.6214×10^{-8}	1.1115×10^{-7}	2.83×10^{-8}	8.34×10^{-7}	1.0×10^{-9}	1000
	4	2.7624×10^{-8}	2.0703×10^{-8}	1.1659×10^{-8}	2.76×10^{-8}	6.47×10^{-6}	1.0×10^{-9}	976

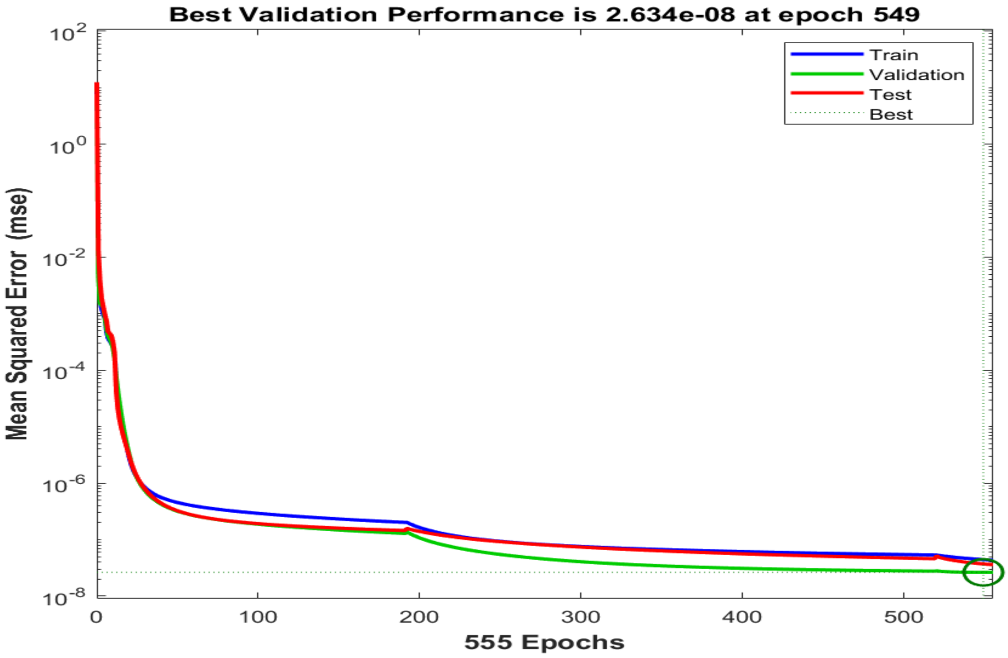

Figure (8a). Performance of the ANN algorithm in terms of MSE.

In ANN, an error or cost function is defined that quantifies the difference between the actual outputs and predicted outcomes with MLP-ANN. A simple measure of the error is MSE. The training results of the designed ANN schemes are illustrated in Fig. 6(a) for scenario 1 of case 1-4. It can be observed that the MSE valuations, which are high in the initial stages of the training sections, reduce with higher values of epochs. Based on the function of the MLP model, MSE values are decreased when the number of iterations is increased, as a result training session of the ANN scheme vanishes as maximum accuracy is reached.

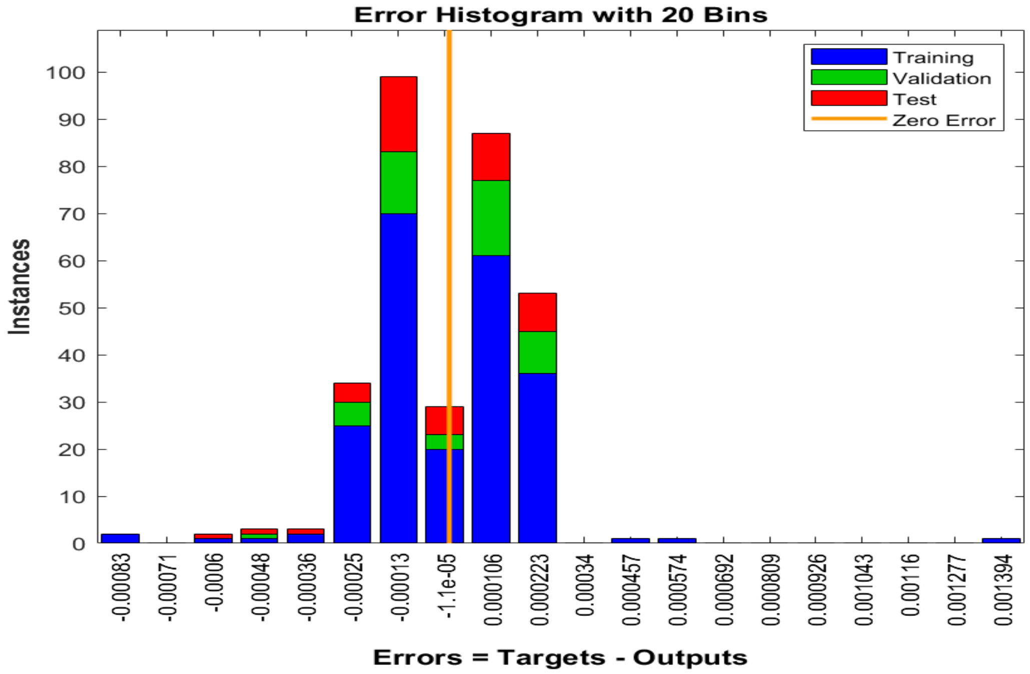

Figure (8b). Error Histogram of ANN Algorithm.

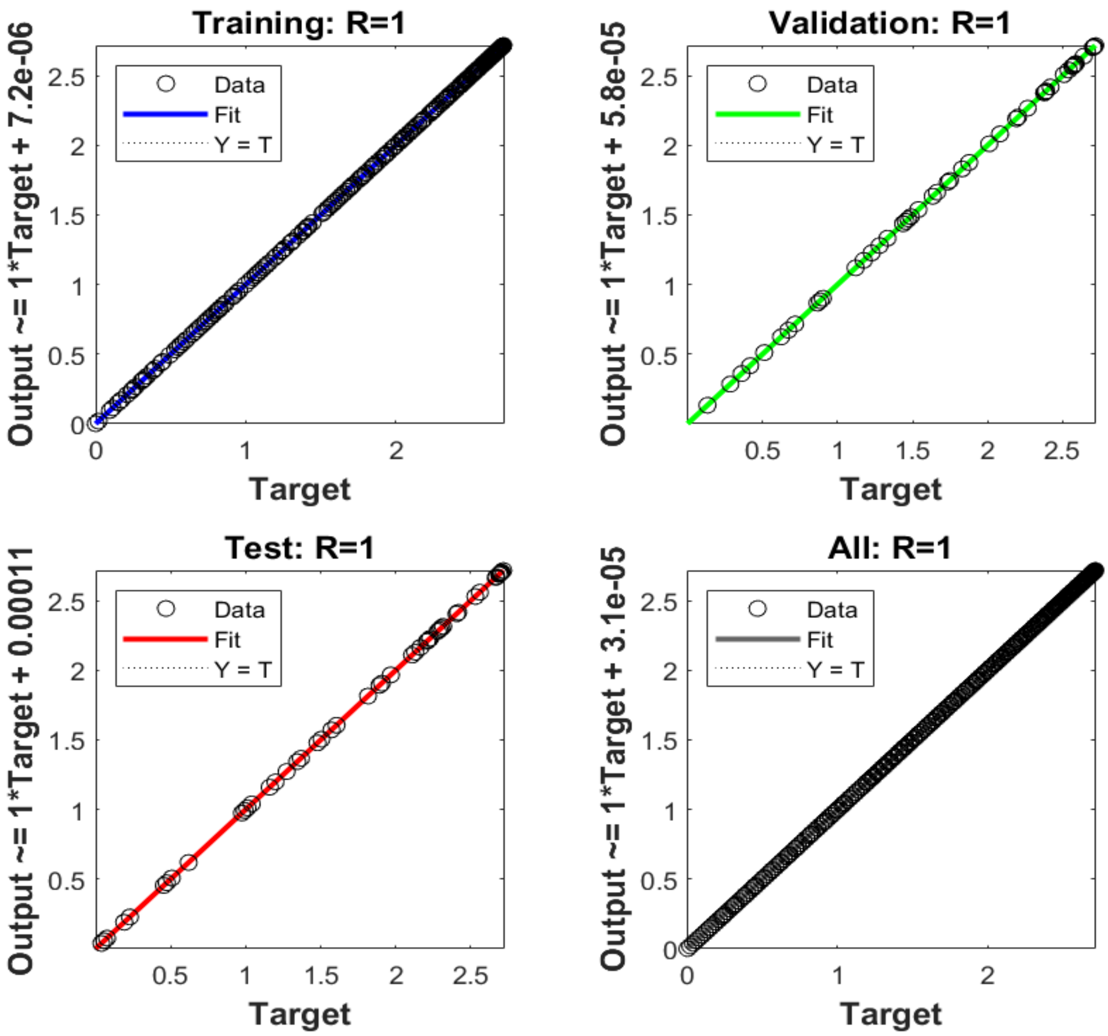

Figure (8c). Linear regression of the ANN Algorithm.

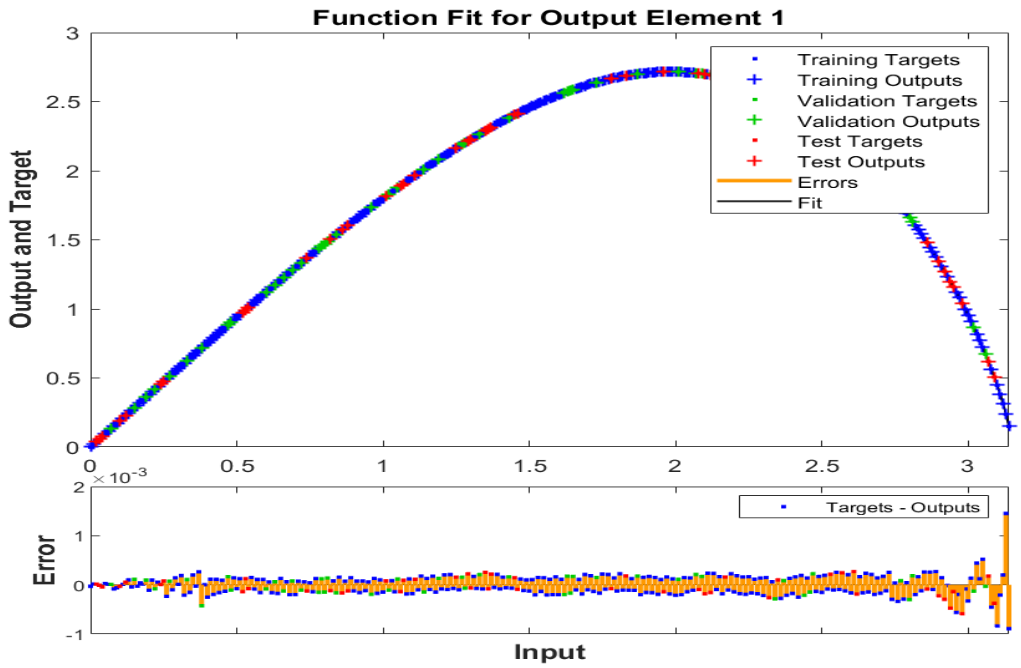

Figure (8d). Fitness function maximum curve with ANN Algorithm.

Figure 8(a-d) are graphically representation of the analysis of data for scenario 3 for case 1.

Table 7: Analogous analysis with ANN for $Gr^{\frac{1}{5}}C_f$ for scenario 4 of case 1-4.

Scenario	Case	MSE Level			Performance	Gradient	Mu	Epoch
		Training	Validation	Testing				
4	1	3.2375×10^{-8}	2.9213×10^{-8}	3.1594×10^{-8}	3.23×10^{-8}	4.12×10^{-6}	1.0×10^{-9}	822
	2	1.5977×10^{-8}	1.0698×10^{-8}	1.6798×10^{-8}	1.6×10^{-8}	6.49×10^{-7}	1.0×10^{-9}	1000
	3	1.9874×10^{-8}	1.0466×10^{-7}	1.9619×10^{-7}	1.99×10^{-8}	9.10×10^{-7}	1.0×10^{-8}	1000
	4	1.1695×10^{-8}	1.0481×10^{-8}	1.4892×10^{-8}	1.17×10^{-8}	8.22×10^{-8}	1.0×10^{-8}	279

Fig. 6(b) addresses the error histogram between the predicted value and the actual value of the numerical data of the proposed non-Newtonian nanofluid over a cylinder. However, it is obtained that numerical evaluations of error presented on the x-axis of plots are minor. The existing situation of data utilized in testing, training, and validation of ANN schemes is presented in Fig. 6(c). The outcomes of the ANN scheme are displayed on the y-axis and the target numerical values on the x-axis. It is noted that there is minimal error observed in the closeness of data points of target and projected values. The fitted line close to the zero line indicates that the average error abruptly declines. The accuracy of an ANN is strongly correlated with R values that are nearly equal to 1. Furthermore, it must be noted that the R values are nearly equal to 1. In Artificial Neural Network (ANN), a function fit plot basically refers to the graphical representation of how the model outputs match the actual outputs during the training or testing phase. Fig. 6(d) visually evaluating the performance of the ANN model. When the graphs are researched, it is observed that the model-predicted output and the actual output are well matched, and the ANN model vanished at almost zero error-line.

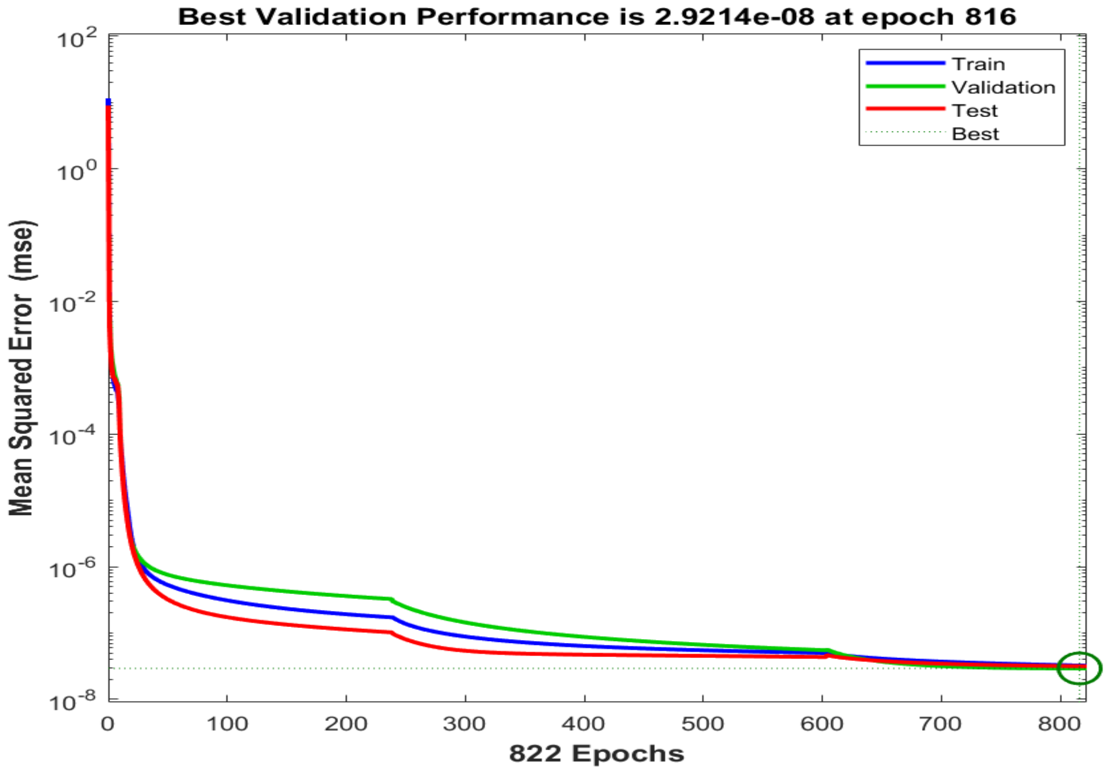

Figure(9a). Performance of the ANN Algorithm in terms of MSE.

a)

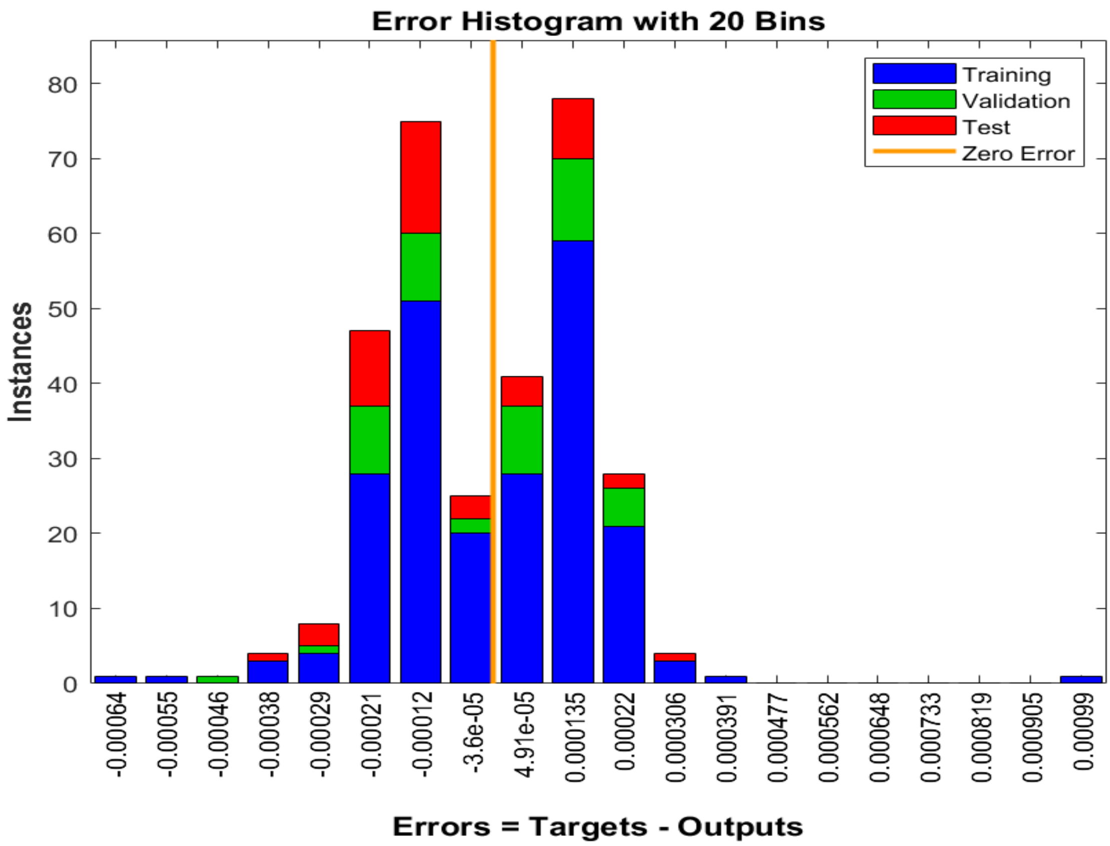

Figure (9b). Error Histogram of ANN Algorithm.

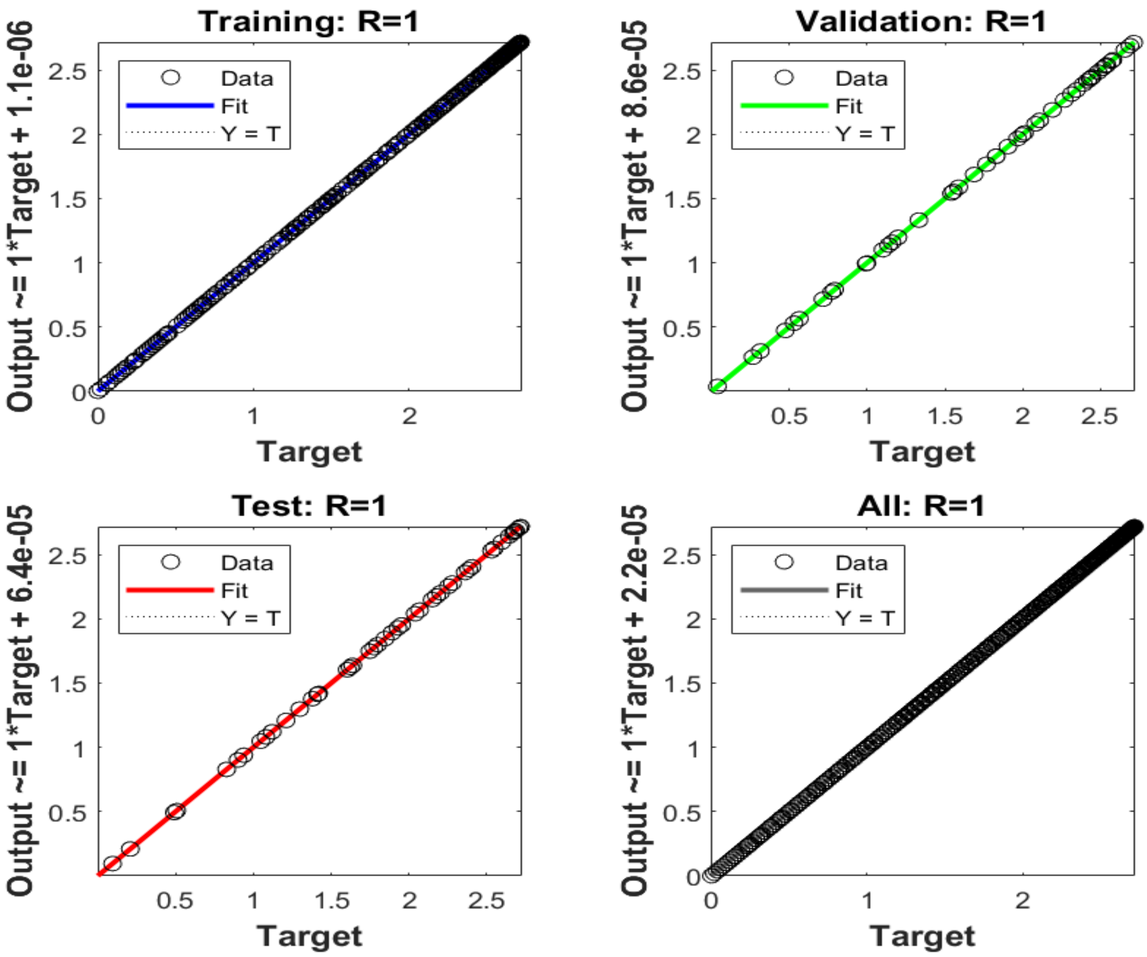

Figure (9c). Linear regression of the ANN Algorithm.

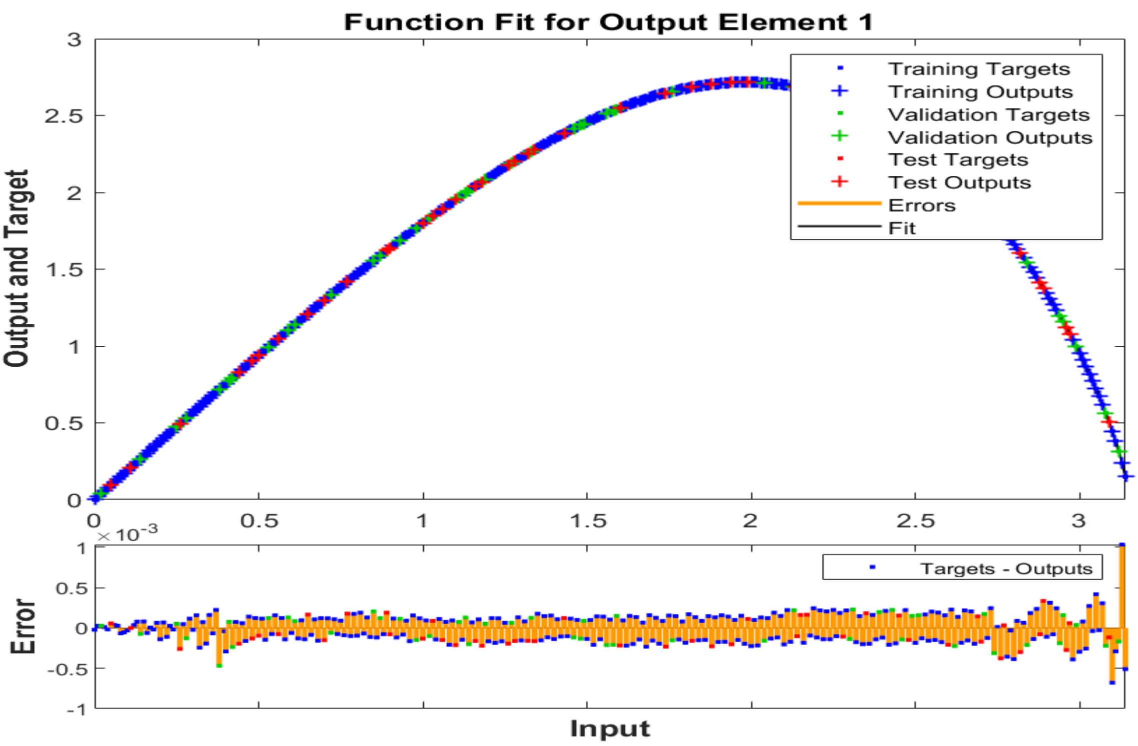

Figure (9d). Fitness function maximum curve with ANN Algorithm.

Figure 9(a-d) shows graphically representation of the analysis of data for scenario 4 for case 1.

Table 8: Analogous analysis with ANN for $Gr^{\frac{1}{5}}C_f$ for scenario 5 of case 1-4.

Scenario	Case	MSE Level			Performance	Gradient	Mu	Epoch
		Training	Validation	Testing				
5	1	4.8198×10^{-8}	2.8228×10^{-8}	4.4960×10^{-8}	4.81×10^{-8}	1.0×10^{-7}	1.0×10^{-8}	787
	2	6.3081×10^{-9}	4.9139×10^{-9}	5.2018×10^{-9}	6.30×10^{-9}	5.98×10^{-7}	1.0×10^{-9}	1000
	3	3.4320×10^{-7}	2.8151×10^{-7}	5.5761×10^{-7}	3.43×10^{-7}	5.98×10^{-5}	1.0×10^{-8}	439
	4	8.4458×10^{-6}	3.7325×10^{-6}	2.3956×10^{-6}	8.44×10^{-6}	1.0×10^{-7}	1.0×10^{-8}	176

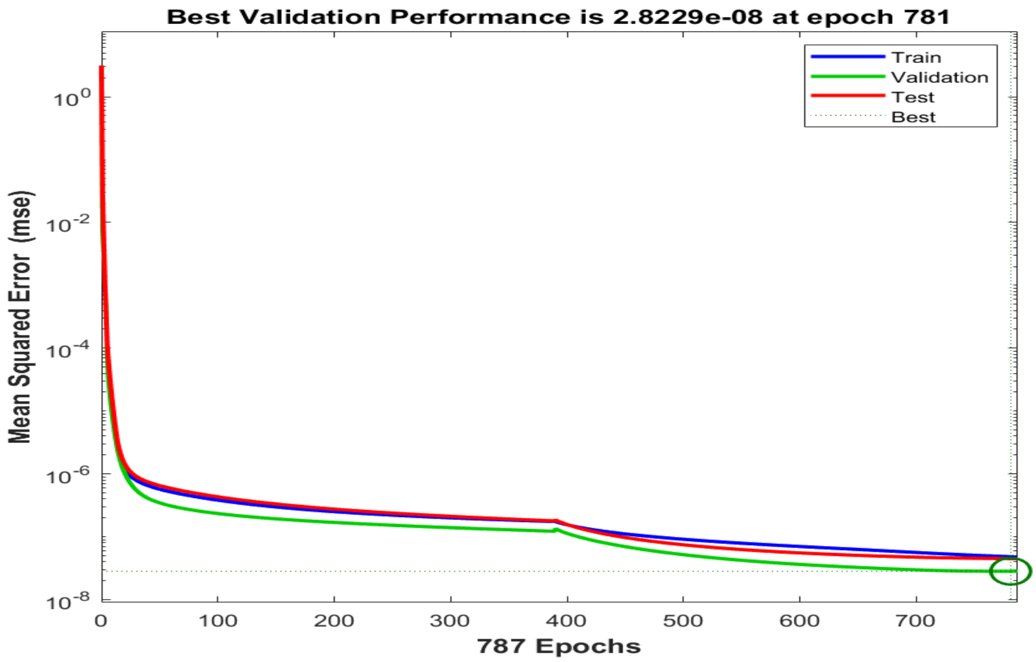

Figure (10a). Performance of the ANN Algorithm in terms of MSE.

Table 5 presents the tabulated values of gradient, Mu, and MSE for cases 1-4 of scenario 2. The performance of MLP-ANN is achieved at 4.8×10^{-8}, 1.1×10^{-8}, 8.15×10^{-8}, and 1.63×10^{-8} against epoch 608, 1000, 1000, and 1000 for cases 1-4 of scenario 2. The numerical values of Mu and gradient for an approximate solution of boundary layer flow characterizing non-Newtonian nanofluid and heat transfer are [1.00×10^{-8}, 1.00×10^{-9}, 1.00×10^{-9}, 1.00×10^{-8}] and [4.24×10^{-5}, 6.50×10^{-8}, 4.19×10^{-7} and 3.88×10^{-8}] for cases 1-4 of scenario 2, respectively. Fig. 7(a) depicts the graphical representation of MSE for scenario 2. Fig. 7(a) displays the convergence of the proposed MLP-ANN model, and it is found that the accuracy is achieved at 10^{-8}. The error histogram is displayed in Fig. 7(b) between predicted and actual values of the proposed fluid model over a cylinder. The accuracy and validity of the predicted solution are computed to be e^{-6}. The correlation index and linear regression for scenario 2 are presented in Fig. 7(c). When the value of the correlation index is close to

1, it shows the best-fitted model. It is noted in Fig. 7(c) that $R = 1$. Fig. 7(d) demonstrates the optimal curve fitness function for scenario 2. It is also demonstrated that the optimal curve fitness function satisfies the boundary condition asymptotically.

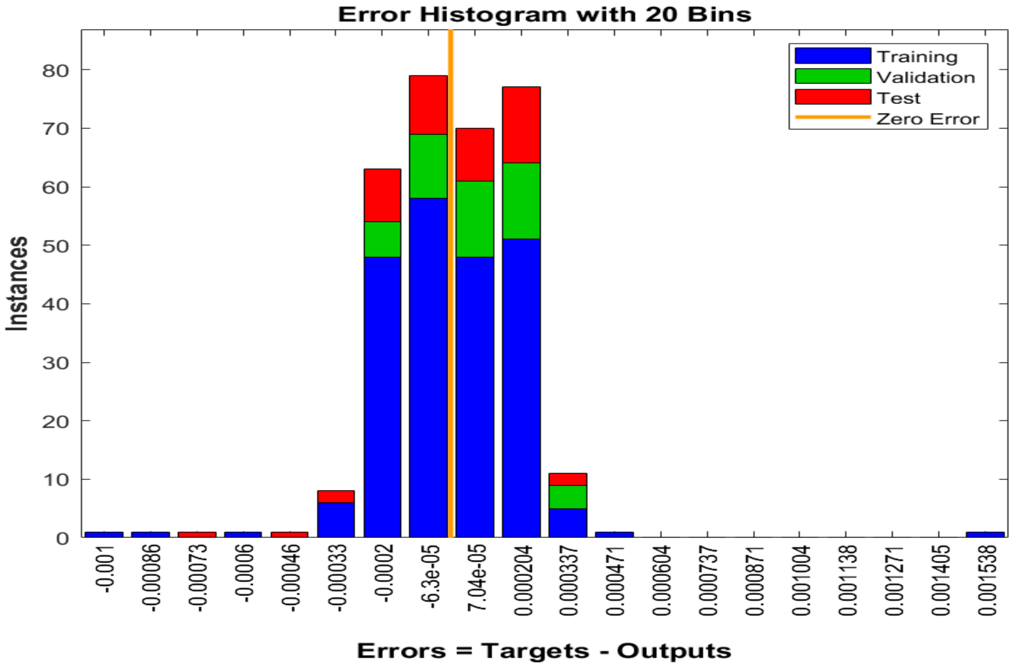

Figure (10b). Error Histogram of ANN Algorithm.

Table 6-8 presents the tabulated values of gradient, Mu, and MSE for cases 1-4 of scenario 3-5. The performance of MLP-ANN is achieved at 4.42×10^{-8}, 3.23×10^{-8}, and 4.81×10^{-8} against epoch 555, 822, and 777 for case 1 of scenario 3-5. The numerical values of Mu and gradient for an approximate solution of boundary layer flow characterizing non-Newtonian nanofluid and heat transfer are [1.00×10^{-9}, 1.00×10^{-7}, 1.0×10^{-8}] and [1.97×10^{-7}, 4.12×10^{-6} and 1.0×10^{-8}] for case 1 of scenario 3-5, respectively. Fig. 8(a)-10(a) portray graphically representation of MSE for scenario 3-5. Error histogram is displayed in Fig. 8(b)-8(b), for scenarios 3-5, respectively. The correlation index and linear regression for scenarios 3-5 are shown in Fig. 8(c)-10(c). The optimal curve fitness function for scenario 3-5 is shown in Fig. 8(d)-10(d). Table 9 presents the detailed data analysis for the Nusselt number against different scenarios as mentioned in Table 3.

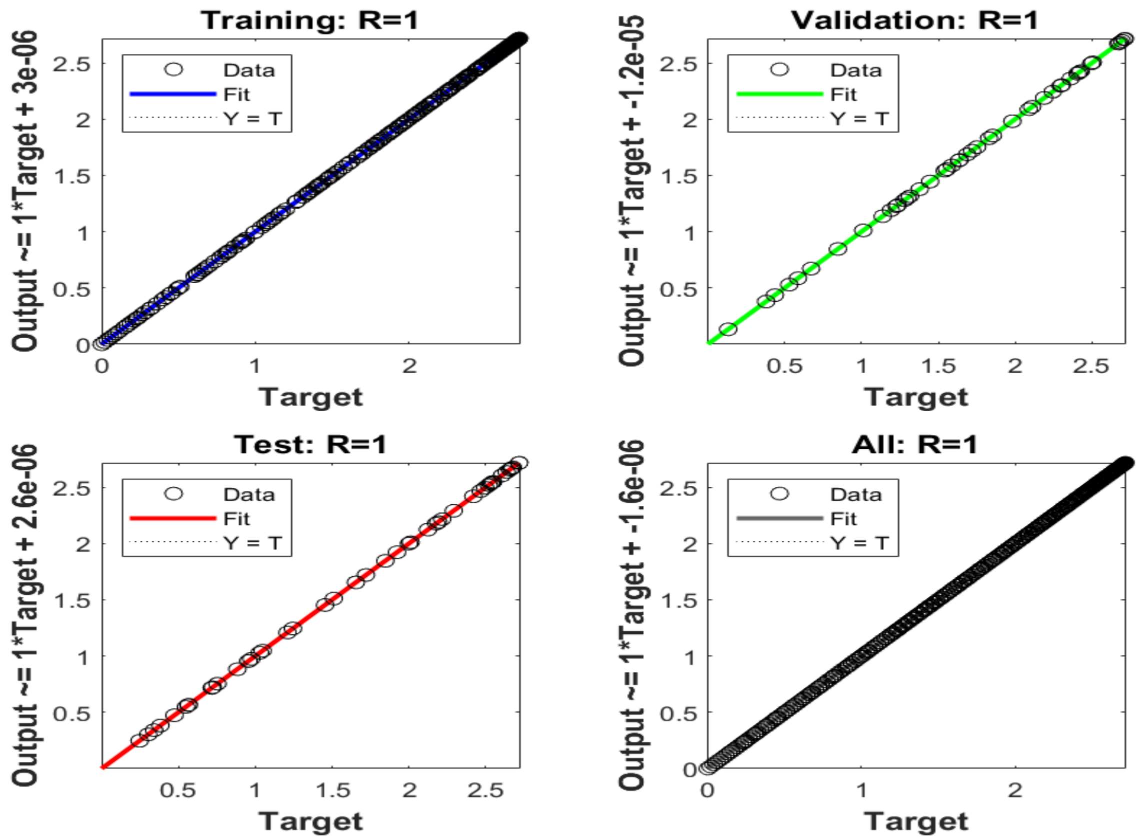

Figure (10c). Linear regression of the ANN Algorithm.

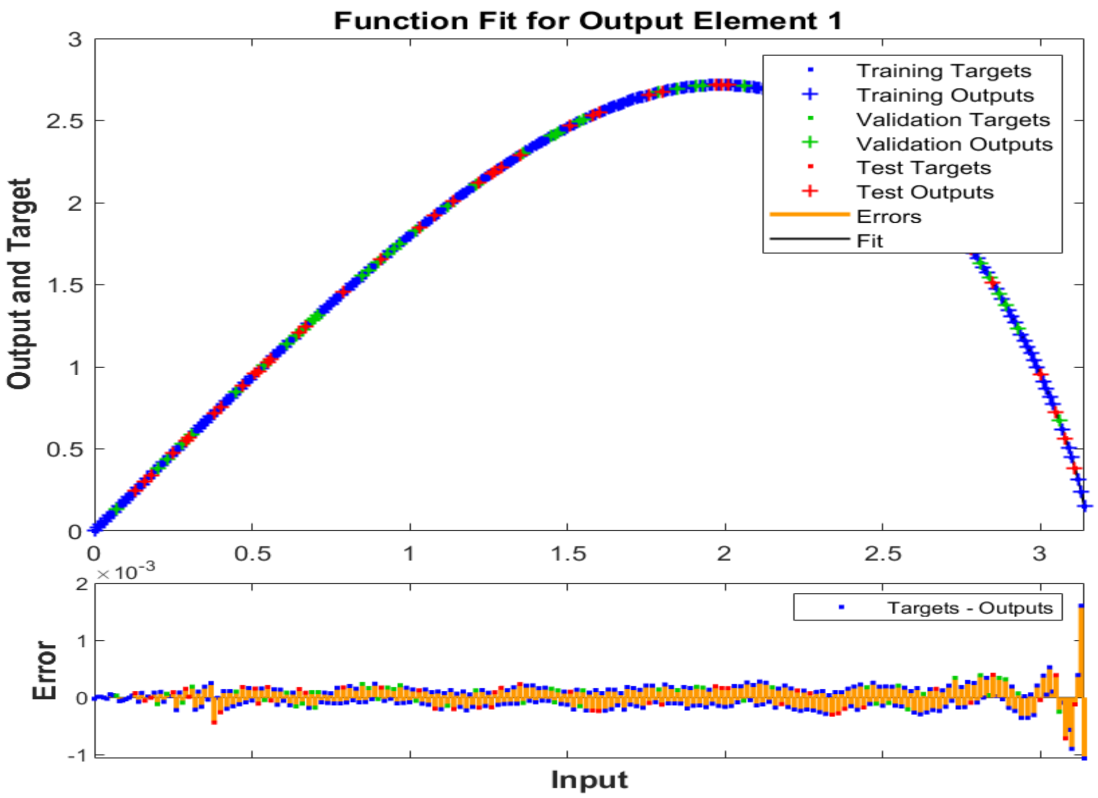

Figure (10d). Fitness function maximum curve with ANN Algorithm.

Figure 10 (a-d) are graphically representation of the analysis of data for scenario 5 for case 1.

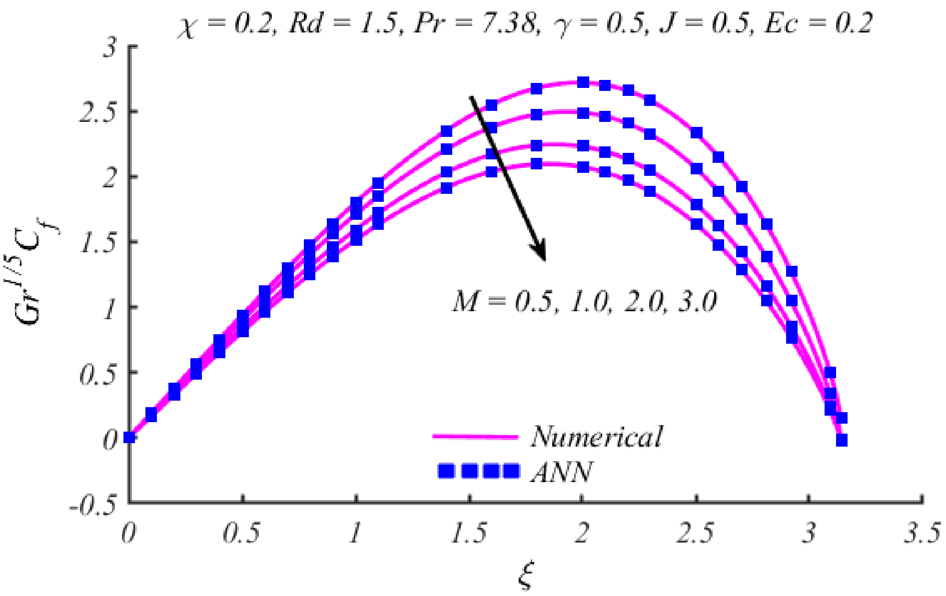

Figure 11. Graphical representation of skin friction for different values of M.

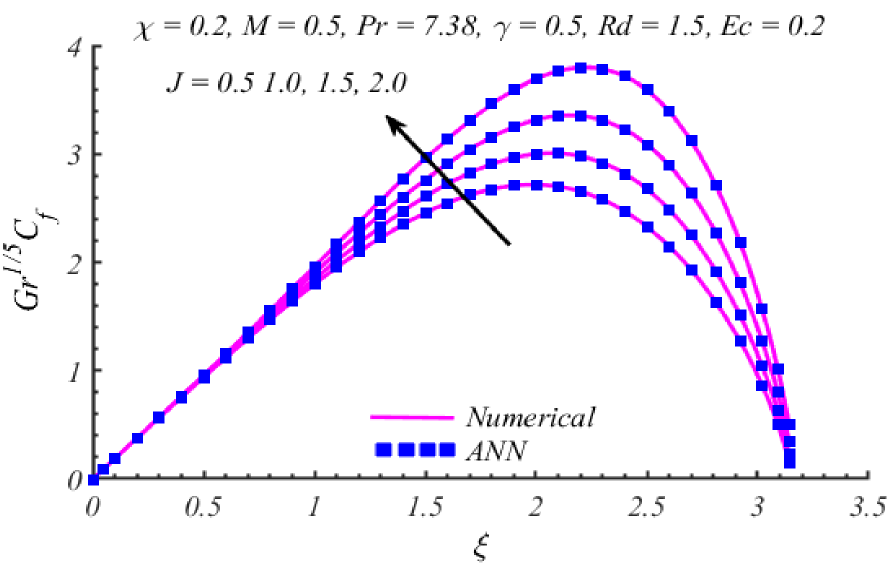

Figure 12. Graphical representation of skin friction for different values of J.

The consequences of magnetic field intensity (M) on drag force ($Gr^{\frac{1}{5}}C_f$) is displayed in Fig. 11. The drag force $Gr^{\frac{1}{5}}C_f$ decreases due to the rise in magnetic field intensity. This phenomenon happens due to the Lorentz force that produces due to magnetic field intensity, which opposes the flow outcomes. Fig. 12 displays the impact of Joule heating parameter (J) on $Gr^{\frac{1}{5}}C_f$. In Fig. 12, it is observed that when the value of J improves, as a result yield stress of the Casson fluid increases, which leads to a reduction in $Gr^{\frac{1}{5}}C_f$. The drag force $Gr^{\frac{1}{5}}C_f$ is analysed against Casson fluid parameter $'\gamma'$ in Fig. 13. It is demonstrated that in Fig. 13, when the value of γ raises then $Gr^{\frac{1}{5}}C_f$ decline. Fig. 14 elaborates the impact of the concentration of nanoparticles on $Gr^{\frac{1}{5}}C_f$. The drag force shows improving behaviour due to a rise in the value of χ. The presence of nanoparticles in a fluid increases the resistance against the flow as a result $Gr^{\frac{1}{5}}C_f$ growing behaviour. Fig. 15 represents the influence of thermal radiation (Rd) on $Gr^{\frac{1}{5}}C_f$. The thermal characteristics increase the flow outcomes, as noted in Fig. 15, when the value of thermal radiation improves as a consequence of the rise in momentum boundary layer. Therefore, we observe an increasing behaviour in $Gr^{\frac{1}{5}}C_f$.

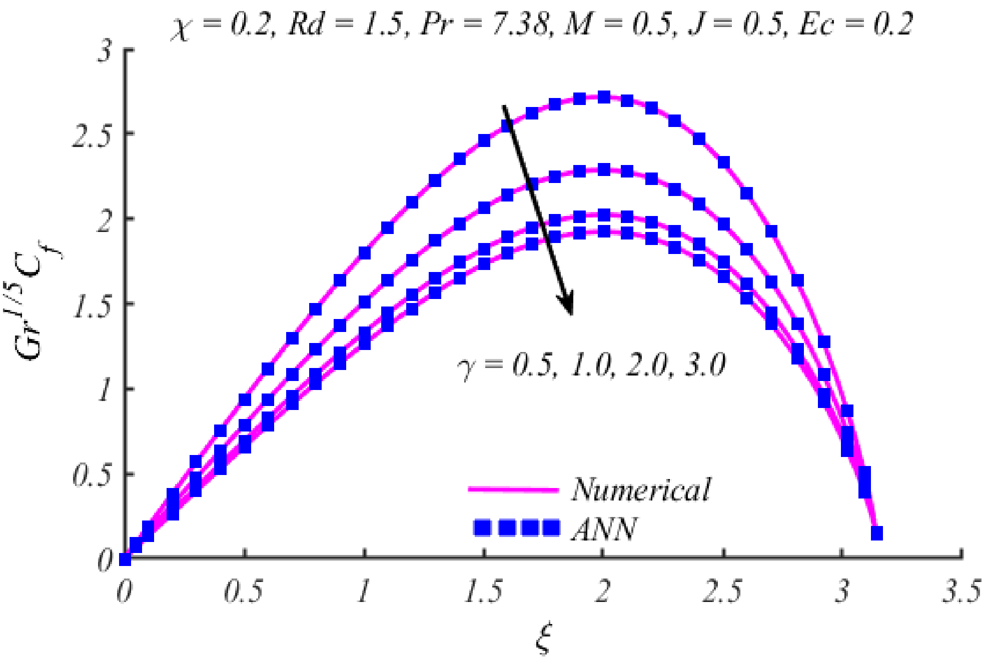

Figure 13. Graphical representation of skin friction for different values of γ.

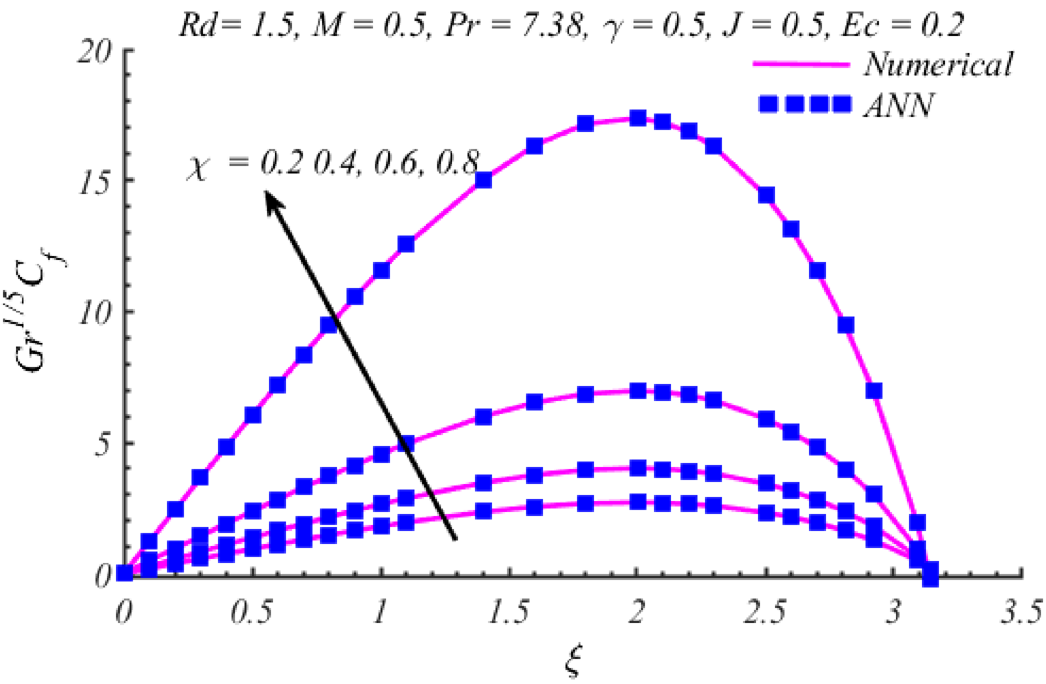

Figure 14. Graphical representation of skin friction for different values of χ.

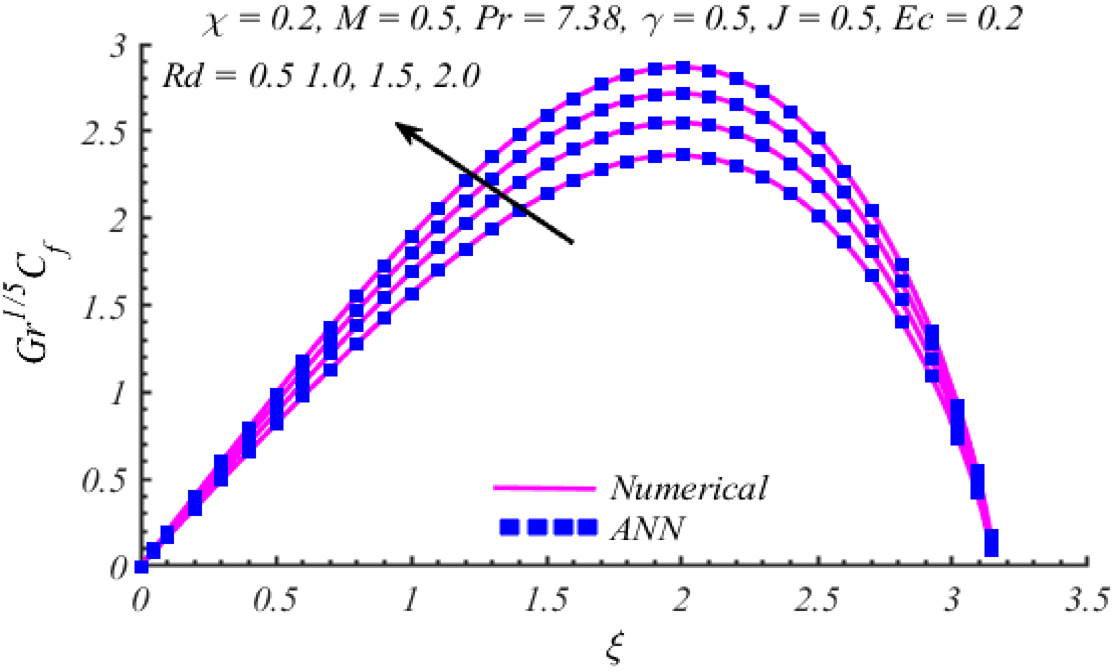

Figure 15. Graphical representation of skin friction for different values of Rd.

Table 9: Analogous analysis with ANN for Nusselt number for scenarios 1-3 of case 1-4.

Scenario	Case	MSE Level			Performance	Gradient	Mu	Epoch
		Training	Validation	Testing				
1	1	8.1670×10^{-9}	9.2233×10^{-9}	7.0639×10^{-9}	8.16×10^{-9}	4.95×10^{-7}	1.0×10^{-10}	201
	2	1.8243×10^{-9}	2.6065×10^{-9}	3.1721×10^{-6}	1.82×10^{-9}	9.93×10^{-8}	1.0×10^{-10}	756
	3	4.9608×10^{-9}	1.5979×10^{-8}	5.7616×10^{-9}	4.96×10^{-9}	9.92×10^{-8}	1.0×10^{-10}	571
	4	1.2363×10^{-8}	1.0209×10^{-8}	7.7527×10^{-9}	1.24×10^{-8}	9.93×8	1.0×10^{-9}	385
2	1	7.3210×10^{-9}	3.2178×10^{-9}	2.9109×10^{-7}	7.32×10^{-9}	7.17×10^{-7}	1.0×10^{-10}	279
	2	5.2315×10^{-9}	1.4571×10^{-8}	3.0750×10^{-8}	5.23×10^{-9}	9.98×10^{-8}	1.0×10^{-10}	833
	3	5.3517×10^{-9}	7.5757×10^{-9}	3.7313×10^{-9}	5.35×10^{-9}	4.75×10^{-7}	1.0×10^{-10}	529
	4	6.3610×10^{-9}	8.1870×10^{-9}	1.6661×10^{-8}	6.36×10^{-9}	9.72×10^{-8}	1.0×10^{-9}	352
3	1	7.2813×10^{-9}	4.0936×10^{-8}	2.4118×10^{-8}	7.28×10^{-9}	9.94×10^{-8}	1.0×10^{-9}	302
	2	6.2996×10^{-9}	8.9980×10^{-9}	1.7103×10^{-8}	6.30×10^{-8}	9.91×10^{-8}	1.0×10^{-10}	358
	3	8.8873×10^{-9}	3.6227×10^{-9}	2.5652×10^{-8}	8.88×10^{-9}	9.94×10^{-8}	1.0×10^{-9}	417
	4	9.5929×10^{-9}	5.6826×10^{-9}	2.7290×10^{-9}	9.55×10^{-9}	3.03×10^{-7}	1.0×10^{-10}	298

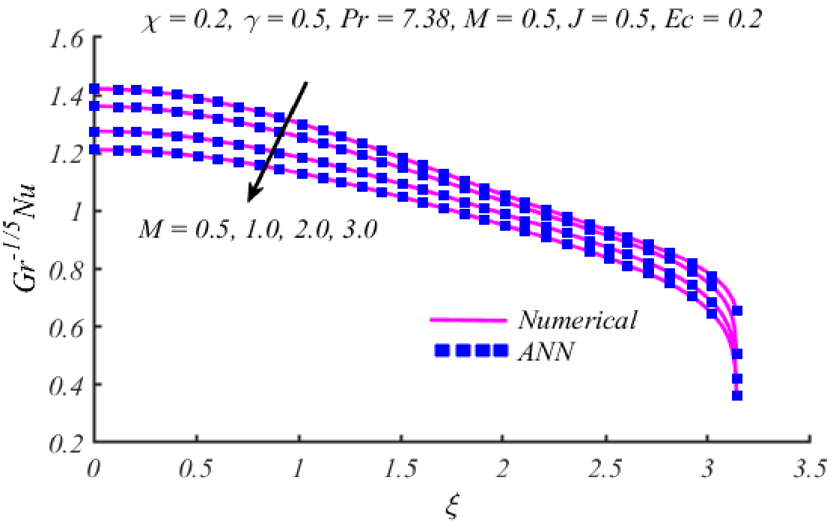

Figure 16. Graphical representation of Nusselt number for different values of M.

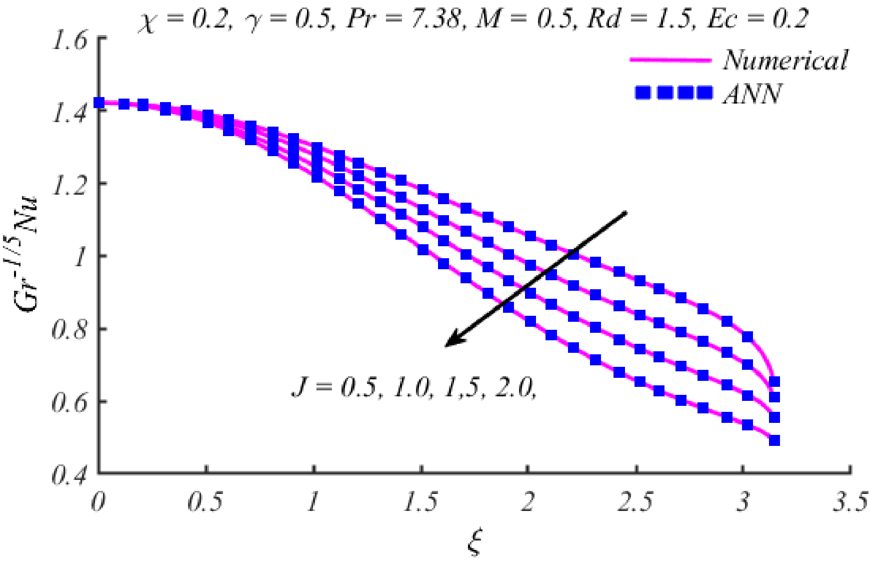

Figure 17. Graphical representation of Nusselt number for different values of J.

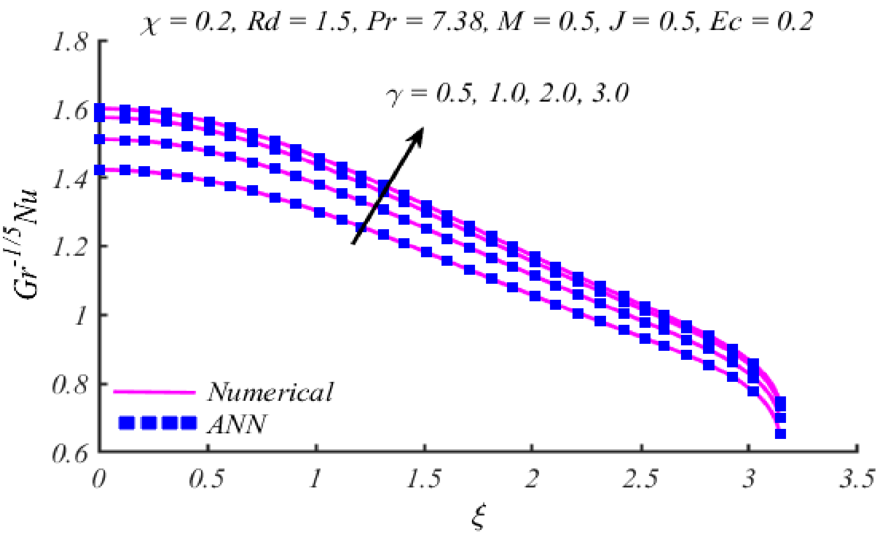

Figure 18. Graphical representation of Nusselt number for different values of γ.

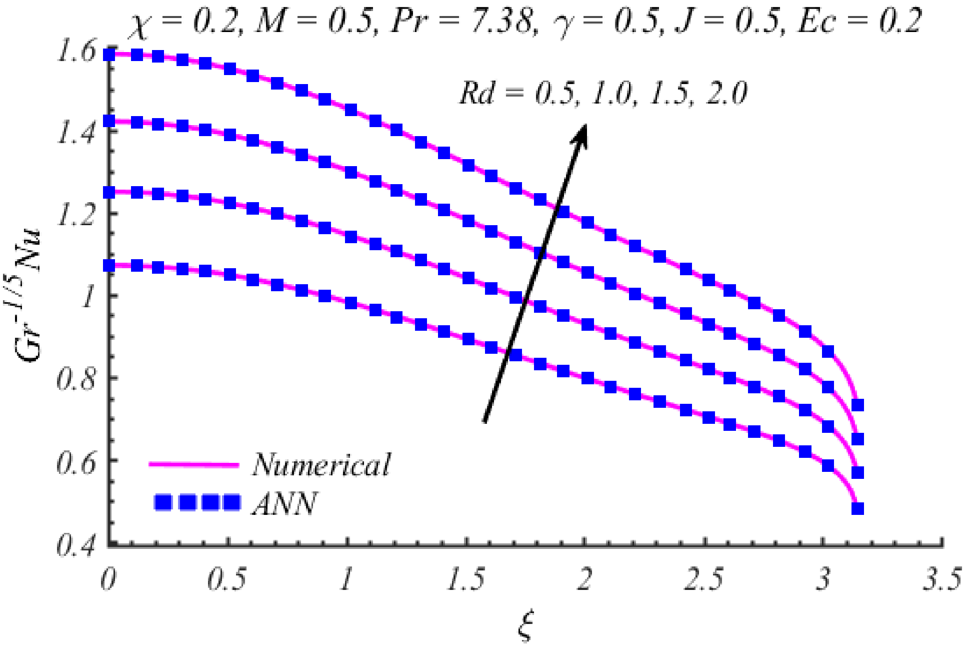

Figure 19. Graphical representation of Nusselt number for different values of Rd.

Fig. 16 depicts the effects of M on Nusselt number ($Gr^{-\frac{1}{5}}Nu$). It is noted that there is a decrease in the value of heat transfer when we face an enhancement in the value of M. This happens due to an increase in the value of the Lorentz force, which oppose transport properties of fluid and heat transfer in a circular cylinder. The consequences of the Nusselt number ($Gr^{-\frac{1}{5}}Nu$). Fig. 17 depicts the effect of J on the Nusselt number $Gr^{-\frac{1}{5}}Nu$. It is noted that when there is an increment in the value of J, we face an improvement in heat transfer $Gr^{-\frac{1}{5}}Nu$. This behaviour is attributed to the fact that larger values of J correspond to increased shear stress of the Casson fluid, resulting in increased rheological effects. Fig. 18 displays the consequences of γ on the Nusselt number $Gr^{-\frac{1}{5}}Nu$. It is seen that as γ increases, the yield stress of Casson fluid decreases, leading to decreases in $Gr^{-\frac{1}{5}}Nu$ increases with higher values of γ. Fig. 19 represents the influence of thermal radiation Rd on Nusselt number ($Gr^{-\frac{1}{5}}Nu$), it is evident that $Gr^{-\frac{1}{5}}Nu$ exhibited a consistent increase with increasing value of the Rd.

5 | CONCLUSION

The present study examines the flow behavior of boundary layer flow of non-Newtonian nanofluid over a horizontal circular cylinder with thermal radiation impact. Numerical solution is evaluated with an implicit finite difference scheme (Keller-Box method). However, the predicted solution is computed with trained MLP-ANN simulation MATLAB software. The efficiency and accuracy of the trained MLP-ANN are simulated with gradient and Mu for the proposed situations. The numerical values of Mu and gradient for an approximate solution of boundary layer flow characterizing non-Newtonian nanofluid and heat transfer are [1.00$\times 10^{-9}$, 1.00$\times 10^{-8}$, 1.00$\times 10^{-9}$, 1.00$\times 10^{-9}$, 1.0$\times 10^{-8}$] and [5.18$\times 10^{-7}$, 1.81$\times 10^{-5}$, 1.97$\times 10^{-7}$, 4.12$\times 10^{-6}$ and 1.0$\times 10^{-7}$] for mention cases in Table 3 for the drag force. For Nusselt number, we have Mu and gradient [1.00$\times 10^{-10}$, 1.00$\times 10^{-10}$, and 1.00$\times 10^{-9}$] and [4.95$\times 10^{-7}$, 7.17$\times 10^{-7}$, and 9.94$\times 10^{-8}$] respectively. The following important points are concluded from the flow observation of Casson nanofluid over a circular cylinder;

- $Gr^{\frac{1}{5}}C_f$ declines with the growing nature of the Casson fluid parameter γ, while $Gr^{-\frac{1}{5}}Nu$ surges as γ improves.
- $Gr^{\frac{1}{5}}C_f$ and $Gr^{-\frac{1}{5}}Nu$ shows a decreasing nature against the growing value of M.
- $Gr^{\frac{1}{5}}C_f$ and $Gr^{-\frac{1}{5}}Nu$ increases as there is an improvement in the value of Rd.
- $Gr^{\frac{1}{5}}C_f$ surges with the growing value of J, while $Gr^{-\frac{1}{5}}Nu$ reduces as the value of J upsurges.

Acknowledgment: We are thankful to the editors and anonymous reviewers for their constructive suggestions.

Author Contributions: Conceptualization, M.S. and M.I.K.; methodology, M.S., M.I.K., and M.I.R.; software, M.S. and M.I.R.; validation, M.S. and M.I.K.; writing, original draft preparation, M.S. and M.I.R.; writing, review, and editing, M.S. and M.I.R. All authors agreed to the manuscript.

Declaration of Conflicting Interest: The author(s) declared no potential conflicts of interest with respect to the research, authorship, and/or publication of this article.

Funding: The author(s) received no financial support for the research, authorship, and/or publication of this article.

Data Availability Statement: Data that supports the findings of this study are available on request from the corresponding author.

Plagiarism Statement: This article was scanned by the plagiarism program. No plagiarism was detected.

Disclaimer/Publisher's Note: The statements, opinions, and data contained in all publications are solely those of the individual author(s) and contributor(s) and not of the publisher "AGASR" and/or the editor(s). The Publisher AGASR and/or the editor(s) disclaim responsibility for any injury to people or property resulting from any ideas, methods, instructions, or products referred to in the content.

REFERENCES

[1] E. Perlman, R. Burns, Y. Li, and C. Meneveau, "Data exploration of turbulence simulations using a database cluster," in *Proceedings of the 2007 ACM/IEEE conference on Supercomputing*, Reno Nevada: ACM, Nov. 2007, pp. 1–11. doi: 10.1145/1362622.1362654.

[2] X. Wu and P. Moin, "A direct numerical simulation study on the mean velocity characteristics in turbulent pipe flow," *J. Fluid Mech.*, vol. 608, pp. 81–112, Aug. 2008, doi: 10.1017/S0022112008002085.

[3] S. L. Brunton and J. N. Kutz, *Data-driven science and engineering: Machine learning, dynamical systems, and control*. Cambridge University Press, 2022.

[4] J. Dominique, J. Van Den Berghe, C. Schram, and M. A. Mendez, "Artificial neural networks modeling of wall pressure spectra beneath turbulent boundary layers," *Phys. Fluids*, vol. 34, no. 3, p. 035119, Mar. 2022, doi: 10.1063/5.0083241.

[5] J. Svorcan, S. Stupar, S. Trivković, N. Petrašinović, and T. Ivanov, "Active boundary layer control in linear cascades using CFD and artificial neural networks," *Aerosp. Sci. Technol.*, vol. 39, pp. 243–249, Dec. 2014, doi: 10.1016/j.ast.2014.09.010.

[6] A. Giannopoulos and J.-L. Aider, "Data-driven order reduction and velocity field reconstruction using neural networks: The case of a turbulent boundary layer," *Phys. Fluids*, vol. 32, no. 9, p. 095117, Sep. 2020, doi: 10.1063/5.0015870.

[7] M. A. Z. Raja, S. Azad, and S. M. Shah, "Bio-inspired computational heuristics to study the boundary layer flow of the Falkner-Scan system with mass transfer and wall stretching," *Appl. Soft Comput.*, vol. 57, pp. 293–314, Aug. 2017, doi: 10.1016/j.asoc.2017.03.047.

[8] M. I. Khan, A. Zeeshan, R. Ellahi, and M. M. Bhatti, "Advanced Computational Framework to Analyze the Stability of Non-Newtonian Fluid Flow through a Wedge with Non-Linear Thermal Radiation and Chemical Reactions," *Mathematics*, vol. 12, no. 10, p. 1420, May 2024, doi: 10.3390/math12101420.

[9] M. Shoaib, M. Kausar, K. S. Nisar, M. Asif Zahoor Raja, and A. Morsy, "Impact of thermal energy on MHD Casson fluid through a Forchheimer porous medium with inclined non-linear surface: A soft computing approach," *Alex. Eng. J.*, vol. 61, no. 12, pp. 12211–12228, Dec. 2022, doi: 10.1016/j.aej.2022.06.014.

[10] M. Awais, M. A. Z. Raja, S. E. Awan, M. Shoaib, and H. M. Ali, "Heat and mass transfer phenomenon for the dynamics of Casson fluid through porous medium over shrinking wall subject to Lorentz force and heat source/sink," *Alex. Eng. J.*, vol. 60, no. 1, pp. 1355–1363, Feb. 2021, doi: 10.1016/j.aej.2020.10.056.

[11] P. B. A. Reddy and R. Das, "Estimation of MHD boundary layer slip flow over a permeable stretching cylinder in the presence of chemical reaction through numerical and artificial neural network modeling," *Eng. Sci. Technol. Int. J.*, vol. 19, no. 3, pp. 1108–1116, Sep. 2016, doi: 10.1016/j.jestch.2015.12.013.

[12] S. L. Brunton, B. R. Noack, and P. Koumoutsakos, "Machine Learning for Fluid Mechanics," *Annu. Rev. Fluid Mech.*, vol. 52, no. 1, pp. 477–508, Jan. 2020, doi: 10.1146/annurev-fluid-010719-060214.

[13] Y. M. Lee, J. H. Lee, and J. Lee, "Artificial neural network-based wall-modeled large-eddy simulations of turbulent channel and separated boundary layer flows," *Aerosp. Sci. Technol.*, vol. 132, p. 108014, Jan. 2023, doi: 10.1016/j.ast.2022.108014.

[14] P. Bala Anki Reddy, S. Jakeer, H. Thameem Basha, S. R. Reddisekhar Reddy, and T. Mahesh Kumar, "Multi-layer artificial neural network modeling of entropy generation on MHD stagnation point flow of Cross-nanofluid," *Waves Random Complex Media*, vol. 35, no. 3, pp. 5215–5242, May 2025, doi: 10.1080/17455030.2022.2067375.

[15] A. Noghrehabadi, R. Mirzaei, M. Ghalambaz, A. Chamkha, and A. Ghanbarzadeh, "Boundary layer flow heat and mass transfer study of Sakiadis flow of viscoelastic nanofluids using hybrid neural network-particle swarm optimization (HNNPSO)," *Therm. Sci. Eng. Prog.*, vol. 4, pp. 150–159, Dec. 2017, doi: 10.1016/j.tsep.2017.09.003.

[16] D. Colorado, M. E. Ali, O. García-Valladares, and J. A. Hernández, "Heat transfer using a correlation by neural network for natural convection from vertical helical coil in oil and glycerol/water solution," *Energy*, vol. 36, no. 2, pp. 854–863, Feb. 2011, doi: 10.1016/j.energy.2010.12.029.

[17] A. Samanta and H. Mondal, "Prediction model based on artificial neural network and bivariate spectral quasi-linearization method for compressible turbulent boundary-layer flow over a smooth flat surface," *Phys. Fluids*, vol. 35, no. 12, p. 125148, Dec. 2023, doi: 10.1063/5.0174985.

[18] M. A. Z. Raja, M. Shoaib, S. Hussain, K. S. Nisar, and S. Islam, "Computational intelligence of Levenberg-Marquardt backpropagation neural networks to study thermal radiation and Hall effects on boundary layer flow past a stretching sheet," *Int. Commun. Heat Mass Transf.*, vol. 130, p. 105799, Jan. 2022, doi: 10.1016/j.icheatmasstransfer.2021.105799.

[19] S. Chakraverty and S. Mall, *Artificial Neural Networks for Engineers and Scientists: Solving Ordinary Differential Equations*, 1st ed. Boca Raton : CRC Press, 2017.: CRC Press, 2017. doi: 10.1201/9781315155265.

[20] P. Sharma, B. K. Sharma, M. Sharma, B. Almohsen, and K. Urbanowicz, "Entropy generation prediction for nanofluid flow using artificial neural networks: a comparative study of training algorithms," *J. Therm. Anal. Calorim.*, vol. 150, no. 18, pp. 14477–14500, Sep. 2025, doi: 10.1007/s10973-025-14489-x.

[21] N. S. Hanspal, B. A. Allison, L. Deka, and D. B. Das, "Artificial neural network (ANN) modeling of dynamic effects on two-phase flow in homogenous porous media," *J. Hydroinformatics*, vol. 15, no. 2, pp. 540–554, Apr. 2013, doi: 10.2166/hydro.2012.119.

[22] A. S. Baazeem, M. S. Arif, and K. Abodayeh, "An Efficient and Accurate Approach to Electrical Boundary Layer Nanofluid Flow Simulation: A Use of Artificial Intelligence," *Processes*, vol. 11, no. 9, p. 2736, Sep. 2023, doi: 10.3390/pr11092736.

[23] K. Khellaf and G. Lauriat, "Numerical study of heat transfer in a non-Newtonian Carreau-fluid between rotating concentric vertical cylinders," *J. Non-Newton. Fluid Mech.*, vol. 89, no. 1–2, pp. 45–61, Feb. 2000, doi: 10.1016/S0377-0257(99)00030-0.

[24] A. Jalali, A. Amiri Delouei, M. Khorashadizadeh, A. M. Golmohamadi, and S. Karimnejad, "Mesoscopic Simulation of Forced Convective Heat Transfer of Carreau-Yasuda Fluid Flow over an Inclined Square: Temperature-dependent Viscosity," *J. Appl. Comput. Mech.*, vol. 6, no. 2, Apr. 2020, doi: 10.22055/jacm.2019.29503.1605.

[25] G. Kumaran, R. Sivaraj, V. R. Prasad, O. A. Beg, and R. P. Sharma, "Finite difference computation of free magneto-convective Powell-Eyring nanofluid flow over a permeable cylinder with variable thermal conductivity," *Phys. Scr.*, vol. 96, no. 2, p. 025222, Feb. 2021, doi: 10.1088/1402-4896/abd121.

[26] P. Loganathan and M. Dhivya, "HEAT AND MASS TRANSFER ANALYSIS OF A CONVECTIVE WILLIAMSON FLUID FLOW OVER A CYLINDER," *Int. J. Fluid Mech. Res.*, vol. 47, no. 2, pp. 171–189, 2020, doi: 10.1615/InterJFluidMechRes.2020027371.

[27] S. Khan *et al.*, "An analytical investigation of the mixed convective Casson fluid flow past a yawed cylinder with heat transfer analysis," *Open Phys.*, vol. 19, no. 1, pp. 341–351, 2021.

[28] R. Nazar, N. Amin, and I. Pop, "Mixed convection boundary-layer flow from a horizontal circular cylinder in micropolar fluids: case of constant wall temperature," *Int. J. Numer. Methods Heat Fluid Flow*, vol. 13, no. 1, pp. 86–109, Feb. 2003, doi: 10.1108/09615530310456778.

[29] A. Subba Rao, C. H. Amanulla, N. Nagendra, O. Anwar Bég, and A. Kadir, "Hydromagnetic Flow and Heat Transfer in a Williamson Non-Newtonian Fluid from a Horizontal Circular Cylinder with Newtonian Heating," *Int. J. Appl. Comput. Math.*, vol. 3, no. 4, pp. 3389–3409, Dec. 2017, doi: 10.1007/s40819-017-0304-x.

[30] Adnan *et al.*, "Enhanced thermal study in hybrid nanofluid flow in a channel motivated by graphene/Fe3O4 and Newtonian heating," *Results Eng.*, vol. 21, p. 101772, Mar. 2024, doi: 10.1016/j.rineng.2024.101772.

[31] D. Khan, G. Ali, P. Kumam, K. Sitthithakerngkiet, and F. Jarad, "Heat transfer analysis of unsteady MHD slip flow of ternary hybrid Casson fluid through nonlinear stretching disk embedded in a porous medium," *Ain Shams Eng. J.*, vol. 15, no. 2, p. 102419, Feb. 2024, doi: 10.1016/j.asej.2023.102419.

[32] T. Anusha, H.-N. Huang, and U. S. Mahabaleshwar, "Two dimensional unsteady stagnation point flow of Casson hybrid nanofluid over a permeable flat surface and heat transfer analysis with radiation," *J. Taiwan Inst. Chem. Eng.*, vol. 127, pp. 79–91, Oct. 2021, doi: 10.1016/j.jtice.2021.08.014.

[33] Ismail, B. S. Bhadauria, A. Kumar, S. K. Rawat, and M. Yaseen, "Thermal instability of Tri-hybrid Casson nanofluid with thermal radiation saturated porous medium in different enclosures," *Chin. J. Phys.*, vol. 87, pp. 710–727, Feb. 2024, doi: 10.1016/j.cjph.2023.12.032.

[34] U. S. Mahabaleshwar, E. H. Aly, and T. Anusha, "MHD slip flow of a Casson hybrid nanofluid over a stretching/shrinking sheet with thermal radiation," *Chin. J. Phys.*, vol. 80, pp. 74–106, Dec. 2022, doi: 10.1016/j.cjph.2022.06.008.

[35] A. Dawar, S. Islam, Z. Shah, and S. R. Mahmuod, "A passive control of Casson hybrid nanofluid flow over a curved surface with alumina and copper nanomaterials: A study on sodium alginate-based fluid," *J. Mol. Liq.*, vol. 382, p. 122018, Jul. 2023, doi: 10.1016/j.molliq.2023.122018.

[36] S. Saleem, B. Ahmad, A. Naseem, M. B. Riaz, and T. Abbas, "Mono and hybrid nanofluid analysis over shrinking surface with thermal radiation: A numerical approach," *Case Stud. Therm. Eng.*, vol. 54, p. 104023, Feb. 2024, doi: 10.1016/j.csite.2024.104023.

[37] A. Abbas *et al.*, "Thermal analysis of AA7075-AA7072/methanol via Williamson hybrid nanofluid model past thin needle: Effects of Lorentz force and irregular heat rise/fall," *Case Stud. Therm. Eng.*, vol. 53, p. 103883, Jan. 2024, doi: 10.1016/j.csite.2023.103883.

[38] N. M. Hafez, E. N. Thabet, Z. Khan, A. M. Abd-Alla, and S. H. Elhag, "Electroosmosis-modulated Darcy–Forchheimer flow of Casson nanofluid over stretching sheets in the presence of Newtonian heating," *Case Stud. Therm. Eng.*, vol. 53, p. 103806, Jan. 2024, doi: 10.1016/j.csite.2023.103806.

[39] Y. Leng *et al.*, "Computational study of magnetized and dual stratified effects on Non-Darcy Casson nanofluid flow: An activation energy analysis," *Case Stud. Therm. Eng.*, vol. 53, p. 103804, Jan. 2024, doi: 10.1016/j.csite.2023.103804.

[40] M. I. Khan, A. Zeeshan, M. B. Arain, A. S. Alqahtani, and M. Y. Malik, "Temporal stability and non-unique solution of reacting Eyring Powell flows over shrinking wedges using neural networks," *Eng. Appl. Artif. Intell.*, vol. 141, p. 109828, Feb. 2025, doi: 10.1016/j.engappai.2024.109828.